The Astrophysical Journal, 824:146 (17pp), 2016 June 20 doi:10.3847/0004-637X/824/2/146

PROPERTIES OF INTERSTELLAR MEDIUM IN INFRARED-BRIGHT QSOs PROBED BY [O I] 63 μm AND [C II] 158 μm EMISSION LINES*

Yinghe Zhao(赵应和)[1,2,3], Lin Yan[1], and Chao-Wei Tsai[4,5]
[1] Infrared Processing and Analysis Center, California Institute of Technology 100-22, Pasadena, CA 91125, USA; zhaoyinghe@gmail.com
[2] Purple Mountain Observatory, Chinese Academy of Sciences, Nanjing 210008, China
[3] Key Laboratory of Radio Astronomy, Chinese Academy of Sciences, Nanjing 210008, China
[4] Jet Propulsion Laboratory, California Institute of Technology, 4800 Oak Grove Dr., Pasadena, CA 91109, USA
Received 2015 May 20; accepted 2016 March 23; published 2016 June 23

ABSTRACT

We present a study of the interstellar medium (ISM) in the host galaxies of nine QSOs at $0.1 < z < 0.2$ with black hole masses of $3 \times 10^7\,M_\odot$ to $3 \times 10^9\,M_\odot$ based on the far-IR spectroscopy taken with *Herschel Space Observatory*. We detect the [O I] 63 μm ([C II] 158 μm) emission in 6 (8) out of 8 (9) sources. Our QSO sample has far-infrared luminosities ($L_{\rm FIR}$) $\sim$several times $10^{11}\,L_\odot$. The observed line-to-$L_{\rm FIR}$ ratios ($L_{[\rm O\,I]63\,\mu m}/L_{\rm FIR}$ and $L_{[\rm C\,II]}/L_{\rm FIR}$) are in the ranges of 2.6×10^{-4} to 10^{-2} and 2.8×10^{-4} to 2×10^{-3}, respectively (including upper limits). These ratios are comparable to the values found in local ULIRGs, but higher than the average value published so far for $z > 1$ IR-bright QSOs. One target, W0752+19, shows an additional broad velocity component ($\sim$720 km s^{-1}) and exceptionally strong [O I] 63 μm emission with $L_{[\rm O\,I]63\,\mu m}/L_{\rm FIR}$ of 10^{-2}, an order of magnitude higher than the average value found among local (U)LIRGs. Combining with the analyses of the Sloan Digital Sky Survey optical spectra, we conclude that the [O I] 63 μm emission in these QSOs is unlikely excited by shocks. We infer that the broad [O I] 63 μm emission in W0752+19 could arise from the warm and dense ISM in the narrow-line region of the central active galactic nucleus. Another possible explanation is the existence of a dense gas outflow with $n_{\rm H} \sim 10^4$ cm^{-3}, where the corresponding broad [C II] emission is suppressed. Based on the far-IR [O I] and [C II] line ratios, we estimate constraints on the ISM density and UV radiation field intensity of $n_{\rm H} \lesssim 10^{3.3}$ cm^{-3} and $10^3 < G_0 \lesssim 10^{4.2}$, respectively. These values are consistent with those found in local Seyfert 1 ULIRGs. In contrast, the gas with broad velocity width in W0752+19 has $n_{\rm H} \gtrsim 10^{4.3}$ cm^{-3} and $G_0 > 10^4$.

Key words: galaxies: active – galaxies: ISM – galaxies: starburst – infrared: galaxies – quasars: general

1. INTRODUCTION

Galaxy formation and evolution is essentially a complex process of interplay between stars, the interstellar medium (ISM), and central black holes. The formation of stars and growth of black holes all require input of the ISM, in the form of either cold molecular or multiphase gas medium. Conversely, feedback from massive young stars and black hole accretion can inject tremendous energy and momentum back into the ISM, influencing the next rounds of star formation and black hole growth. Therefore, a comprehensive picture of galaxy formation requires good understanding of stars, the ISM, and central black holes.

The ISM in a galaxy can have several different phases—cold molecular gas, warm neutral gas, and ionized gas. The warm, neutral gas medium is an important part of the galaxy ISM. It can be effectively probed by ionic and atomic forbidden fine-structure emission lines in the far-infrared, transitions such as [C II] 158 μm and [O I] 63 and 145 μm lines. These lines are important coolants for the warm, neutral ISM. Furthermore, [C II] 158 μm is the brightest far-infrared line in most galaxies and accounts for 0.1%–1% of the total far-IR (FIR) luminosity (e.g., Stacey et al. 1991; Malhotra et al. 2001; Díaz-Santos et al. 2013; Sargsyan et al. 2014). The [O I] 63 μm emission can be brighter than the [C II] emission when FIR color, f_{60}/f_{100} (i.e., the 60–100 μm ratio), is larger than $\sim$0.7 (e.g., Malhotra et al. 2001; Brauher et al. 2008). Finally, FIR fine-structure line ratios between [C II] 158 μm and [O I]63 μm and 145 μm lines can also provide critical diagnostic tools for inferring physical conditions of the ISM, such as temperature, density, and intensity of the radiation field, by comparing observational results with model predictions of photodissociation regions (PDRs; e.g., Tielens & Hollenbach 1985; Kaufman et al. 1999; Fischer et al. 2014).

For many years, such detailed studies of the neutral ISM using FIR fine-structure line ratios have been only possible for the Galactic star-forming regions and nearby galaxies in the local group. The observations from *Infrared Space Observatory* (*ISO*; Kessler et al. 1996, 2003) have revealed for the first time that [C II]-to-FIR ratios of nearby normal galaxies are an order of magnitude higher than that of local ultraluminous infrared galaxies (ULIRGs; $L_{\rm IR} > 10^{12}\,L_\odot$) (Malhotra et al. 2001; Luhman et al. 2003; Brauher et al. 2008). The exact physical explanations for this difference are still a topic for debate (Malhotra et al. 2001; Abel et al. 2009; Díaz-Santos et al. 2013).

The advent of the Atacama Large Millimeter/submillimeter Array (ALMA) has made [C II] the most utilized emission line for studying high-z galaxies at millimeter wavelengths. The available ALMA frequencies and its extremely high sensitivity have produced an explosion in the number of [C II] line detections among various types of objects at high redshifts, including star-forming galaxies, active galactic nuclei (AGNs), submillimeter-selected galaxies (SMGs), and QSOs (e.g., Swinbank et al. 2012; Wang et al. 2013; Willott et al. 2013; Decarli et al. 2014; Capak et al. 2015). However, it is

* *Herschel* is an ESA space observatory with science instruments provided by European-led Principal Investigator consortia and with important participation from NASA.
[5] NASA Postdoctoral Program Fellow.

challenging to detect multiple FIR fine-structure lines of low-redshift objects from the ground because of the limited atmospheric windows.

Herschel Space Observatory (Pilbratt et al. 2010) provides the perfect spectral coverage, resolution, and sensitivities for observations of FIR fine-structure lines from galaxies at low redshifts, which are too distant/faint for *ISO* and not accessible from ALMA. *Herschel* has already assembled a large FIR spectroscopic data set for local (U)LIRGs (Díaz-Santos et al. 2013; Farrah et al. 2013; Zhao et al. 2013, 2016; Lu et al. 2014; Sargsyan et al. 2014). Similar studies for $z > 4$ QSOs have been done using IRAM telescopes and ALMA (Maiolino et al. 2005; Gallerani et al. 2012; Venemans et al. 2012; Wagg et al. 2012; Leipski et al. 2013; Wang et al. 2013; Willott et al. 2013). However, there is a lack of similar observations for IR-bright QSOs at low redshifts.

Therefore, it is important to increase the number of low-z QSOs with FIR fine-structure line observations of low-z QSOs. Even with a small increase in the number, such a study can provide insight into how the ISM of QSOs/galaxies evolves from low to high luminosity, and from low z to high z. Here we report our results of the [C II] 158 μm and [O I] 63 μm line observations for nine IR-bright QSOs at $z \sim 0.1$–0.2, taken with the Photodetector Array Camera and Spectrometer (PACS; Poglitsch et al. 2010) on board *Herschel*. The sample is selected using both the Sloan Digital Sky Survey (SDSS) and the *Wide Infrared Survey Explorer* (*WISE*) (Wright et al. 2010).

In this paper, we present our PACS spectra of these two lines, extract line and continuum fluxes, and fit the infrared spectral energy distributions (SEDs) for these QSOs. We also compare our line-to-FIR continuum ratios with other types of galaxies and PDR models. The paper is organized as follows: we describe our sample selection, observations, and data reduction in Section 2, present our results and discussion in Section 3, and summarize briefly in the last section. Throughout the paper, we adopt a Hubble constant of $H_0 = 71\,\mathrm{km\,s^{-1}\,Mpc^{-1}}$, $\Omega_\mathrm{M} = 0.27$, and $\Omega_\Lambda = 0.73$ (Spergel et al. 2007).

2. SAMPLE, OBSERVATIONS, AND DATA REDUCTION

2.1. The IR-bright QSO Sample

The IR-bright QSOs studied in this paper were identified by using the optical spectra from SDSS and drawn from the overlapping sky region between *WISE* and SDSS DR7 data. The SDSS QSO catalog from the 7th data release (Schneider et al. 2010) was used as the initial input. The IR-bright QSOs are selected according to the following: (1) their SDSS redshifts are in the range of 0.1 and 0.2; (2) the observed *WISE* *W*4 flux (i.e., at 22 μm; hereafter f_{W4}), $f_{W4} > 100$ mJy. The first criterion with the narrow redshift slice was chosen so that the major cooling line [C II] 158 μm is still well within the sensitive part of the PACS spectral coverage. The second criterion ensures that the selected sources are bright enough for FIR spectroscopy (their 100 μm fluxes $f_{100} \geqslant 300$ mJy based on local QSO templates). There are only nine sources that satisfy these criteria, and the details of the full sample are listed in Table 1.

2.2. Herschel/PACS FIR Spectroscopy

The PACS spectroscopic data for all but one source (W1659+18; see Table 1), whose [C II] observation was performed by the program OT1_dweedman_1 (PI: D. Weedman), were collected as the OT2 program (ID: OT2_lyan_5; PI: L. Yan), awarded with about 24 hr of observing time. The observations were carried out between 2012 September and 2013 February (see Table 1) using the Integral Field Spectrometer (IFS). The IFS on PACS can perform simultaneous spectroscopic observations in the 51–73 μm or 71–105 μm and the 103–220 μm ranges. The integral field unit is composed of a 5×5 array of individual detectors (spaxels), which has a projected field of view of $47'' \times 47''$ on the sky. The FWHM of the point-spread function (PSF) for the PACS IFS is $\sim 9\farcs5$ between 60 μm and $\sim$110 μm and increases to $\sim 14''$ by 200 μm. The spectral resolution is around 55 km s^{-1} (the third grating order; $\sim$160 km s^{-1} for the second grating order) and 210 km s^{-1} for [O I] 63 μm and [C II], respectively, allowing us to resolve the [O I] and most [C II] lines in velocity (see below).

At $z \sim 0.1$–0.2, an individual PACS spaxel corresponds to $\sim$19–32 kpc, and thus the single pointed observation mode was used for all sources in our sample, with targets placed in the central spaxel. The [O I] 63 μm and [C II] 158 μm lines (Table 1) were observed separately using the line spectroscopy mode. For each line observation, an additional spectral window (red/blue for [O I]/[C II]) was observed simultaneously for the continuum measurement. We used the standard chopping-nodding observing mode, in which the source is observed by alternating between the on-source position and a clean off-source position, and adopted the chopper throw of "Large" (6′; except for the [C II] observation of W1659+18, in which a medium throw of 3′ was used) in order to avoid possible contamination of the background from nearby sources. To eliminate the telescope background emission, two nod positions were used.

The PACS data reduction was performed in the Herschel Interactive Processing Environment version 12.1 (Ott 2010) using a customized chop/nod background normalization pipeline script, which is particularly aimed at fainter sources with long-duration observations. The final spectra were extracted from the central spaxel and corrected for aperture loses using a point-source PSF. All of our sources are unresolved at 22 μm in the *WISE* images. Since 22 μm *WISE* images have an angular resolution of $\sim 12''$, similar to that of PACS at 170 μm, and dust emissions at 20–160 μm generally have similar concentrations (e.g., Muñoz-Mateos et al. 2009), we do not expect significant extended emission outside the adopted aperture. Indeed, we found that the summed spectra from the central 3×3 spaxels are generally consistent with those extracted from the central spaxel (both after aperture correction), but much noisier due to the different continuum slopes. The PACS spectra for our nine targets are shown in Figure 1.

We fitted the observed profile and continuum simultaneously using a single- or two-component Gaussian plus a first-order polynomial. The fitting results are illustrated in Figure 1 using (green) solid lines. Table 2 lists the measured line fluxes, as well as the intrinsic line widths, which have been corrected for the instrumental spectral resolution. We used $\sigma_\mathrm{true} = \sqrt{\sigma^2_\mathrm{obs} - \sigma^2_\mathrm{inst}}$ to make this correction. If a line is not detected, we list its upper limit, which was calculated as 3σ times the spectral resolution (FWHM of the instrumental profile) at the expected wavelength of the line.

The continuum flux was estimated to be the median value of the spectrum (after removing the fitted line profile for the line-

Table 1
The Sample and PACS Observation Log

Galaxy (1)	R.A. (J2000) (2)	Decl. (J2000) (3)	Redshift (4)	Line[a] (5)	Exposure (s)[b] (6)	ObsID (7)	Obs Date (8)
W0752+19	07 52 17.84	+19 35 42.3	0.1170	[O I]/[C II]	384 × 10 × 2/344 × 6	1342251203/35	2012 Sep 19/20
W0946+13	09 46 52.58	+13 19 53.9	0.1332	[O I]/[C II]	384 × 10 × 2/344 × 4	1342256250/49	2012 Nov 29
W1005+43	10 05 41.87	+43 32 40.4	0.1788	[O I]/[C II]	368 × 10 × 2/344 × 5	1342254963/64	2012 Nov 12
W1117+44	11 17 06.40	+44 13 33.3	0.1437	[O I]/[C II]	384 × 10 × 2/344 × 3	1342256771/72	2012 Dec 03
W1355+20	13 55 50.20	+20 46 14.5	0.1965	[O I]/[C II]	368 × 10 × 2/344 × 3	1342259618/19	2013 Jan 14/15
W1422+29	14 22 30.34	+29 52 24.2	0.1133	[O I]/[C II]	384 × 10 × 2/344 × 3	1342262004/05	2013 Jan 24
W1519+52	15 19 07.33	+52 06 06.1	0.1378	[O I]/[C II]	384 × 10 × 1/344 × 5	1342262538/39	2013 Jan 29
W1634+20	16 34 59.83	+20 49 36.1	0.1285	[O I]/[C II]	384 × 10 × 2/344 × 4	1342263467/66	2013 Feb 10
W1659+18[c]	16 59 39.77	+18 34 36.8	0.1709	[O I]/[C II]	384 × 10 × 2/344 × 2	1342263468/38910	2013/12 Feb 10

Notes. Column (1): source; columns (2) and (3): R.A. and decl.; column (4): optical redshift from SDSS DR 10; column (5): targeted line for the corresponding observation ID; column (6): exposure time; column (7): observation ID; column (8): observation date.
[a] At the same time, a different spectrum window was observed for the continuum, as shown in Figure 1.
[b] Time per repetition × number of repetitions per nod cycle (× number of nod cycles). Only the science time is shown, and the on-source exposure time is half of the listed number.
[c] Observations for the [C II] were performed by the program OT1_dweedman_1 (PI: D. Weedman).

emission window), and the error (σ) was calculated using 1.48 × MAD assuming normally distributed noise, where MAD is defined as the median value of the absolute deviations from the median data. Continuum fluxes are listed in Table 3. For the continuum flux below our sensitivity, we give the 3σ flux as an upper limit. We note that the observed spectra with $\lambda = 190$–$220\,\mu$m are in the leakage region and contaminated by spectral features from 95 to 110 μm. Hence, the measured continuum flux within this wavelength range could be overestimated by a factor of three.[6]

2.3. Optical Spectroscopy

The analyses in this paper use the QSO optical spectra taken by SDSS. These spectra provide information on [O I]$\lambda\lambda$6300, 6364 emission lines, which are complementary to the FIR [O I] 63 μm lines observed by *Herschel*/PACS. The reduced, calibrated, one-dimensional SDSS spectra, as well as the three-color RGB images (based on the *g*, *r*, and *i* images; Lupton et al. 2004), are obtained from the SDSS Date Release 10 (Ahn et al. 2014) via the Science Archive Server.[7] In Figures 2(a) and (b), we show the SDSS spectra and RGB images for our sample objects with detections and nondetections of the [O I] $\lambda\lambda$6300, 6364 emissions, respectively.

To obtain the fluxes of the [O I]$\lambda\lambda$6300, 6364 and Hα lines, we fitted the continuum, [O I]$\lambda\lambda$6300, 6364, Hα [N II]$\lambda\lambda$6548, 6583, and [S II]$\lambda\lambda$6716, 6731 simultaneously. During the fitting process, we adopted Gaussian profiles for line emissions, up to two components (narrow and broad) for the [O I]$\lambda\lambda$6300, 6364 lines, and up to four components (one narrow and three broad) for the Hα line. As shown in Shen et al. (2011), a multicomponent fitting to the Hα line generally gives a better-fitted result. The ratio of the [N II]$\lambda\lambda$6548, 6583 doublet is fixed as 1/3. We also assumed that each doublet has the same line width. The best-fitted results (red lines) and residuals (arbitrarily shifted vertically; cyan lines) are also superposed in Figures 2(a) and (b). For a clearer visualization of the [O I] $\lambda\lambda$6300, 6364 doublet, the zoomed spectrum of 6220–6420 Å (rest frame) is plotted in the inset of each panel, with the fitted (if any) individual component(s) overlaid. We also used the similar method to fit the Hβ and [O III]$\lambda\lambda$4959, 5007 lines.

3. RESULTS AND DISCUSSION

3.1. IR Spectral Energy Distribution

To estimate the IR/FIR properties of our sample QSOs, such as the total infrared luminosity ($L_{\rm IR}$; 8–1000 μm), FIR luminosity ($L_{\rm FIR}$; 42.5–122.5 μm), and the fractional contributions to the total $L_{\rm FIR}$ from starburst (SB) activities ($f_{\rm SB}$), we also compiled near-IR (NIR) to FIR photometries from Two Micron All Sky Survey (2MASS), *WISE*, and *IRAS* catalogs, and we list the results in Table 4. Combined with our own PACS spectrophotometric results, these data allow us to obtain the aforementioned parameters ($L_{\rm FIR}$, $L_{\rm IR}$) in a uniform manner by fitting the observed IR SEDs.

To fit the observed IR SEDs, we adopted a simple two-component method, i.e., by combining an SB component and a QSO component. For each component, we allow its fractional contribution to the total SED to vary from 0 (thus only one component) to 1. The SED templates were adopted from the SWIRE library (Polletta et al. 2007), which includes six SBs (NGC 6090, NGC 6240, M82, Arp 220, IRAS 22491-1808, and IRAS 20551-4250) and five QSOs. Among these QSO templates, three of them (QSO1, TQSO1, and BQSO1) represent optically selected QSOs with different values of infrared/optical flux ratios, and two are type 2 QSOs (QSO2 and Torus).

The final algorithm we used to fit the SEDs is similar to that proposed in Sawicki (2012), which properly treats nondetections. Equation (A10) in Sawicki (2012) is used to calculate the χ^2, namely,

$$\chi^2 = \sum_i \left(\frac{f_{{\rm o},i} - f_s f_{{\rm m},i}}{\sigma_i} \right)^2 - 2 \sum_j \ln \left\{ \sqrt{\frac{\pi}{2}}\,\sigma_j \left[1 + {\rm erf}\left(\frac{f_{{\rm lim},j} - f_s f_{{\rm m},j}}{\sqrt{2}\,\sigma_j} \right) \right] \right\}. \quad (1)$$

[6] See https://nhscsci.ipac.caltech.edu/workshop/DP_Workshop_Aug_2013/PACS/presentations/pipeline.pdf.
[7] http://dr10.sdss3.org

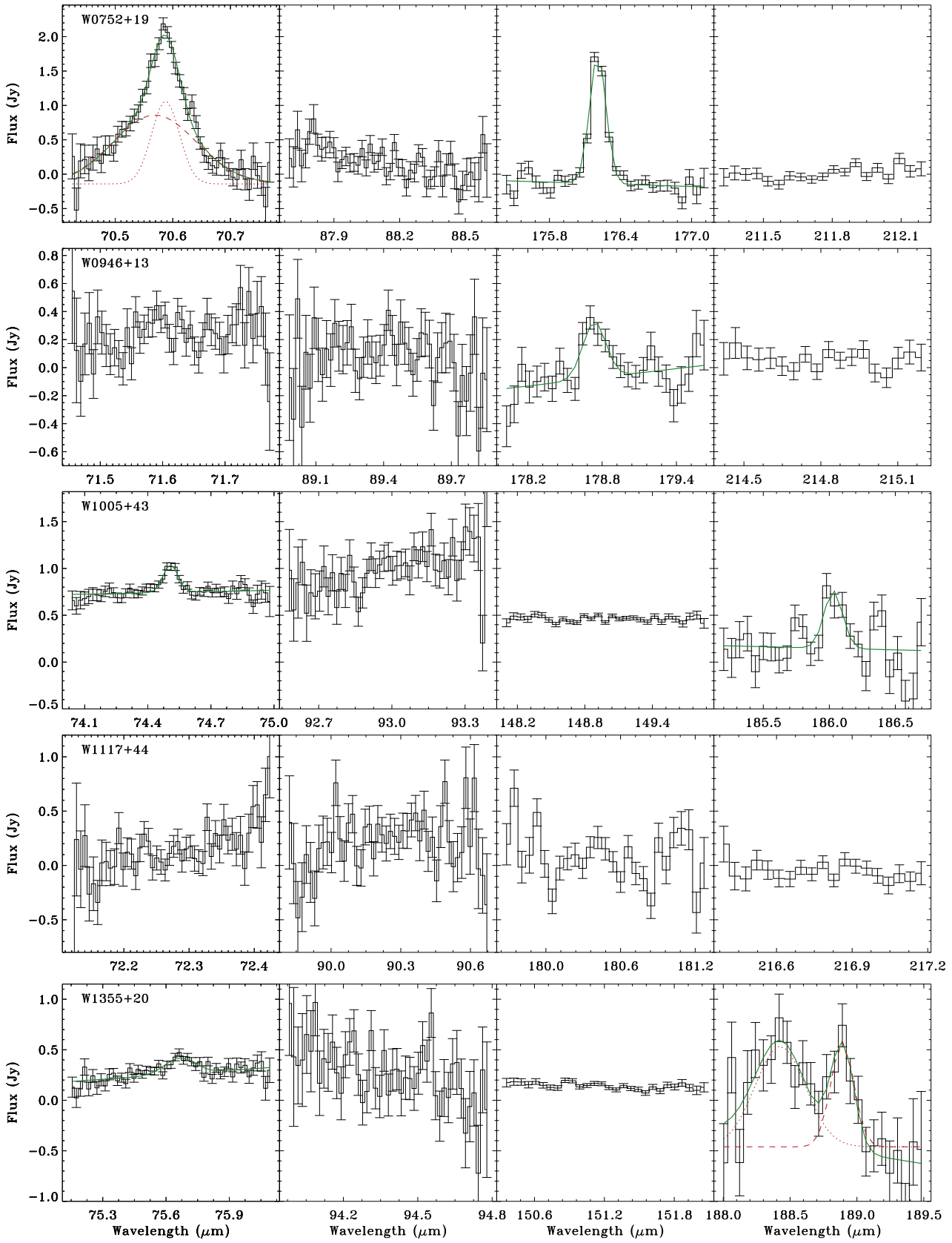

Figure 1. PACS spectra for our QSOs in the observed frame (black). The panels with the range of x-axis within 70–76 μm and 175–190 μm show the [O I] and [C II] lines, respectively, and the other two panels display the continuum. For the line emission, we suppose the fitted (pseudo-)continuum and emission line (thick green) if a line was detected, and individual components (shifted arbitrarily in y-axis) are shown with (red) dashed and dotted lines, respectively, if two components fitting for a line applied.

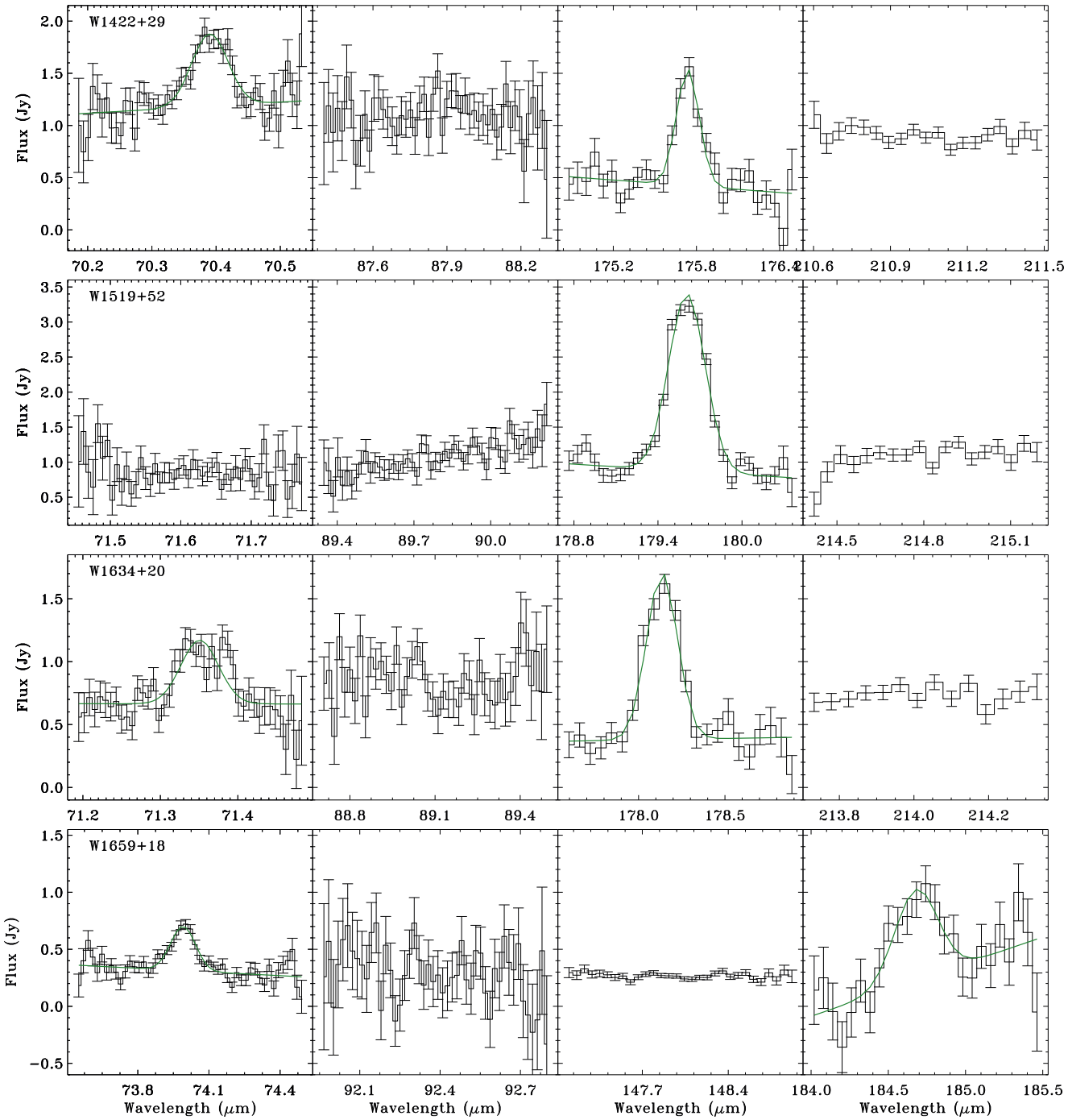

Figure 1. (Continued.)

where $f_{o,i}$ refers to the observed flux density of the detected band i, $f_{\mathrm{lim},j}$ the 1σ flux detection threshold in the jth band, f_{m} the model flux, σ the uncertainty, f_s the scaling factor between the observed data and the model, and $\mathrm{erf}(x)$ the error function.

Figure 3 shows the observed data points and best-fit SEDs for our sample QSOs. In each panel, we plotted SB (dashed line) and QSO (dotted line) components and labeled the name (s) of the best-fitted template(s). The gray lines in each panel give all model results at the 95% confidence level. The combination of the two types of templates fits our observed SEDs generally well. The fitted parameter space is better constrained by having detections at the FIR bands. For three objects (W1422+29, W1519+52, and W1634+20), the data points at the longest wavelength fall in the leakage region and can be overestimated. Thus, we discarded these points during the fitting process. Table 5 lists the derived parameters, such as L_{IR}, L_{FIR}, f_{SB}, and FIR color (f_{60}/f_{100}) from the best-fit SEDs.

3.2. Our Sample of IR-bright QSOs Are Mostly Composite Systems

The L_{IR} values derived from the SED fitting are in the range of (4.6–18.6) $\times$ $10^{11}L_{\odot}$ for our sample (Table 5), similar to

Table 2
Measured Line Fluxes

Galaxy	[O I] 63 μm			[C II] 158 μm			[O I] λ6300		
	Flux	FWHM	Redshift	Flux	FWHM	Readshift	Flux	FWHM	Readshift
W0752+19	4.37 ± 0.34	232	0.1172	3.14 ± 0.27	198	0.1171	624.0 ± 6.2	372	0.1171
W0752+19	11.0 ± 1.4	724	0.1169	<1.10[a]	⋯	⋯	1380 ± 3.1	1335	0.1167
W0946+13	<0.46	⋯	⋯	0.88 ± 0.18	311	0.1331	235.2 ± 5.3	319	0.1330
W0946+13	⋯	⋯	⋯	⋯	⋯	⋯	825.3 ± 2.6	1823	0.1336
W1005+43	1.41 ± 0.13	318	0.1793	0.93 ± 0.30	187	0.1794	<26.9	⋯	⋯
W1117+44	<0.67	⋯	⋯	<0.68	⋯	⋯	<90.2	⋯	⋯
W1355+20	1.48 ± 0.30	664	0.1976	1.88 ± 0.41	262	0.1975	<35.0	⋯	⋯
W1355+20	⋯	⋯	⋯	3.95 ± 1.18	676	0.1945	⋯	⋯	⋯
W1422+29	2.97 ± 0.33	276	0.1141	2.22 ± 0.21	264	0.1141	37.0 ± 4.4	147	0.1143
W1422+29	⋯	⋯	⋯	⋯	⋯	⋯	313.3 ± 2.4	924	0.1139
W1519+52[b]	⋯	⋯	⋯	7.68 ± 0.51	474	0.1386	20.1 ± 4.6	143	0.1382
W1519+52	⋯	⋯	⋯	⋯	⋯	⋯	94.2 ± 3.3	692	0.1385
W1634+20	1.81 ± 0.30	230	0.1293	2.80 ± 0.27	295	0.1293	32.1 ± 2.4	362	0.1291
W1634+20[c]	⋯	⋯	⋯	⋯	⋯	⋯	151.9 ± 5.3	3022	0.1304
W1659+18	2.79 ± 0.34	487	0.1711	2.18 ± 0.22	441	0.1709	157.9 ± 1.5	608	0.1711

Notes. Fluxes are in units of 10^{-17} W m^{-2}, and FWHM in units of km s^{-1}. The second line of each source, if it exists, gives the information of the second component of the emission.
[a] This flux limit was calculated by assuming that the [C II] has the same line width as the [O I] broad component.
[b] The observed spectra do not cover the expected wavelength of the [O I] line for this source.
[c] This component suffers a large uncertainty due to the worse quality of the spectra within this wavelength range, and thus is not taken into account in our analysis.

Table 3
PACS Spectrophotometric Results

Galaxy	PACS1 λ_1	PACS2 λ_2	PACS3 λ_3	PACS4 λ_4
W0752+19	<318	<744	<252	<201
	70.60	88.15	176.27	211.76
W0946+13	<474	<552	<282	<156
	71.61	89.42	178.83	214.81
W1005+43	738 ± 43	983 ± 198	461 ± 45	<702
	74.50	92.99	148.98	185.95
W1117+44	<624	<735	<582	<231
	72.27	90.25	180.48	216.78
W1355+20	252 ± 84	<879	138 ± 35	<660
	75.62	94.38	151.21	188.71
W1422+29	1182 ± 153	1105 ± 213	468 ± 148	912 ± 105[a]
	70.36	87.85	175.68	211.04
W1519+52	852 ± 240	1048 ± 239	820 ± 167	1103 ± 164[a]
	71.61	89.78	179.54	214.83
W1634+20	642 ± 121	840 ± 217	397 ± 122	728 ± 61[a]
	71.34	89.10	178.24	214.03
W1659+18	317 ± 71	<891	268 ± 26	<864
	74.02	92.38	148.01	184.74

Note. For each source, the first line lists the fluxes, and the second line gives the corresponding wavelengths (observed frame). Fluxes are in units of mJy, and wavelength in units of μm.
[a] The observed spectra with $\lambda > 190\,\mu$m are in the leakage region and contaminated by spectral features from 95 to 110 μm. Hence, the measured flux should be overestimated.

(U)LIRGs. The difference from local ULIRG galaxies is that these IR-bright QSOs have very warm FIR colors with f_{25}/f_{60} ratios of 0.14–0.63 (median value of 0.41), typical values seen among *IRAS*-discovered IR-bright QSOs/AGNs. The f_{60}/f_{100} FIR colors are very similar, ∼0.93, as shown in Table 5. We evaluate our full sample with regard to the SB component contribution fraction $f_{\rm SB}$, and we find that it varies from 0 (i.e., complete QSO SED) to 1 (complete SB SED) in the sample. We found that four systems are AGN dominated with $f_{\rm SB} < 0.5$, and the remaining five QSOs are SB dominated with $f_{\rm SB} > 0.5$. The median $f_{\rm SB} = 0.55$ indicates both SB and QSO contributions to their IR luminosities. We note that our QSOs have a factor of 5–10 less FIR emission ($L_{\rm FIR} \sim$ few times $10^{11}\,L_{\odot}$) than that of local ULIRGs. This is expected since these sources are not very bright in *IRAS* catalogs.

The nature of SB-QSO composite SEDs in our sample is consistent with the optical morphologies, as shown in Figures 2(a) and (b), where SDSS color images clearly reveal the extended emissions from host galaxies. Bright IR emissions in excess of a pure QSO template in these sources could be due to dust-obscured star formation in their host galaxies. This is consistent with the fact that the QSO bolometric luminosities, derived from 5100 Å luminosities (Shen et al. 2011), are almost all less than our SED-derived total IR luminosities, $L_{\rm bol}^{\rm QSO} < L_{\rm IR}$. Monochromatic luminosity at 5100 Å is usually measured from an optical spectrum, which is dominated by the light from the central accreting black hole (QSO); therefore, the derived $L_{\rm bol}^{\rm QSO}$ represents mostly the QSO, but not its host galaxy.

3.3. Physical Characteristics of the ISM in Our IR-bright QSOs

The [O I] 63 μm emission arises exclusively from the neutral phase of gas clouds because atomic oxygen has an ionization potential just above 13.6 eV. Although the [C II] line is considered a primary tracer of PDRs (Tielens & Hollenbach 1985), it can also come from diffused, ionized gas as it only takes ∼11.3 eV to form C^+. Neutral and ionized gas can be heated by a photoelectric process (PE; Tielens & Hollenbach 1985) and then cooled via collisional excitation of C^+, O, and other elements. The [O I] 63 μm emission has a higher excitation temperature (∼228 K) and considerably higher critical density (in this paper, all densities are for hydrogen nuclei, not electrons, unless otherwise stated) ($n_{\rm cr} \sim 5 \times 10^5$ cm^{-3}) than that of [C II] emission (92 K and $\sim 3 \times 10^3$ cm^{-3}, respectively). The cooling rate per volume is $\propto n_{\rm gas}^2$ when

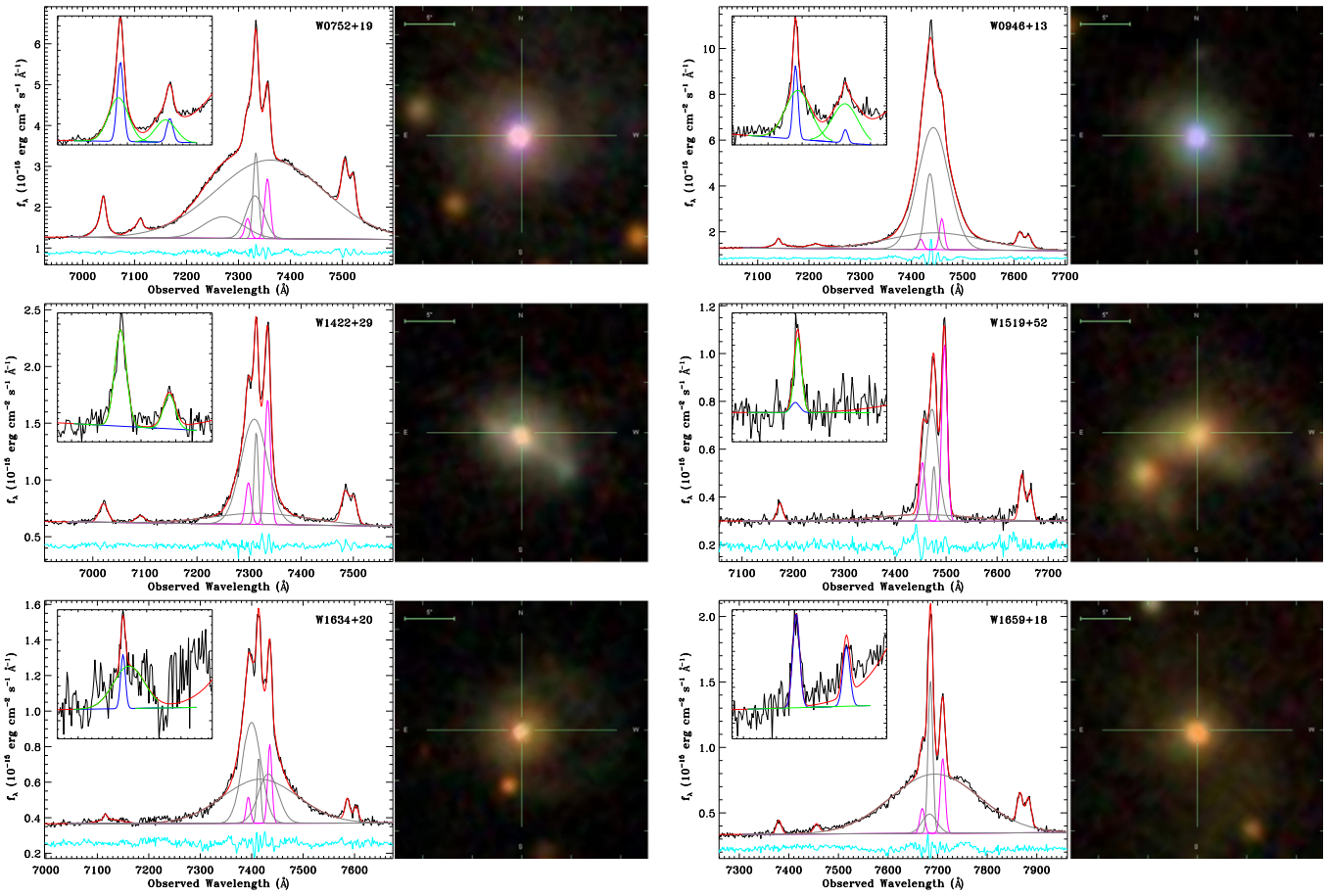

Figure 2. (a) SDSS optical spectra around the Hα line, and false color images (R: *i* band; G: *r* band; B: *g* band) of the QSOs in our sample with at least one line of the [O I]$\lambda\lambda$6300, 6364 doublet detected. For each source, the observed and best fitted spectra are shown by the black and red lines, respectively, with the cyan line (arbitrarily shifted vertically) giving the residuals. Individual components of the Hα line and the [N II]$\lambda\lambda$6548, 6583 doublet (plus the pseudo-continuum) are shown by the gray and magnetar lines, respectively. The inset in each spectrum panel presents an enlarged view of the [O I]$\lambda\lambda$6300, 6364 emissions, with the narrow and broad components (plus the pseudo-continuum) shown by the blue and green lines, respectively. (b) Same as Figure 2(a), except for that the [O I]$\lambda\lambda$6300, 6364 emissions only show very weak features or nondetections.

$n_{\rm gas} < n_{\rm cr}$ and $\propto n_{\rm gas}$ when $n_{\rm gas} > n_{\rm cr}$. On the other hand, the heating rate per volume always increases faster than $n_{\rm gas}$ so that temperature is higher at higher densities. Therefore, the combination of the [C II] 158 μm and [O I] 63 μm lines allows unique determination of the physical properties (e.g., temperature and density) of PDR gas (Kaufman et al. 1999). Furthermore, the ratio of the combined luminosity of these two lines to the IR continuum can be used as a proxy for the PE heating efficiency (e.g., Tielens & Hollenbach 1985), which represents the far-ultraviolet (FUV) energy that goes into the gas, divided by the FUV energy deposited in dust grains.

3.3.1. $L_{[O\ I]63\ \mu m}$-to-$L_{\rm FIR}$ and $L_{[C\ II]}$-to-$L_{\rm FIR}$ Ratios

Table 5 lists the derived line luminosities ($L_{[\rm O\,I]63\,\mu m}$ and $L_{[\rm C\,II]}$, respectively) and line-to-$L_{\rm FIR}$ ratios for our sample. The $L_{[\rm O\,I]63\,\mu m}/L_{\rm FIR}$ values are in the range of 2.6×10^{-4} to 10^{-2} with a median value of 5.2×10^{-4}, including the two upper limits. The $L_{[\rm C\,II]}/L_{\rm FIR}$ ratios span between 2.8×10^{-4} and 2.0×10^{-3} with a median of 7.6×10^{-4}. Figure 4 plots the [O I]-to-FIR (left panel) and [C II]-to-FIR (right panel) luminosity ratios as a function of $L_{\rm FIR}$. For comparisons, we include samples of local normal galaxies (including LIRGs; Brauher et al. 2008), local ULIRGs (Brauher et al. 2008; Farrah et al. 2013), $z > 1$ SMGs (Maiolino et al. 2009; Ivison et al. 2010; De Breuck et al. 2011; Valtchanov et al. 2011; Coppin et al. 2012; Swinbank et al. 2012; Wagg et al. 2012; Riechers et al. 2013), star-forming galaxies/composite systems (Stacey et al. 2010; Brisbin et al. 2015), and $z > 1$ AGNs/QSOs (Pety et al. 2004; Maiolino et al. 2005; Stacey et al. 2010; Gallerani et al. 2012; Venemans et al. 2012; Wagg et al. 2012; Leipski et al. 2013; Wang et al. 2013; Willott et al. 2013).

Figure 4 illustrates one important feature—the line-to-luminosity ratios are broadly dependent on $L_{\rm FIR}$ and have very large variations at a given luminosity and redshift. This large variation probably has to do with variations of ISM properties. For our sample, the $L_{[\rm O\,I]63\,\mu m}/L_{\rm FIR}$ and $L_{[\rm C\,II]}/L_{\rm FIR}$ ratios are similar to that of local ULIRGs. This is not surprising because the $L_{\rm FIR}$ of our QSOs are only a factor of 2–5 smaller than that of local ULIRGs and $L_{[\rm O\,I]63\,\mu m}/L_{\rm FIR}$ and $L_{[\rm C\,II]}/L_{\rm FIR}$ ratios have intrinsic large scattering. However, we find that the line-to-luminosity ratios of our $z \sim 0.15$ AGNs are significantly higher than that of AGNs/QSOs at $z \sim 1$–6 (blue and purple symbols). We emphasize that this statement is not true for all high-z AGNs in general, only true for these high-z AGNs whose infrared luminosities are two orders of magnitude higher than our QSOs. This is due to the fact that the published FIR spectroscopy of high-z QSOs is largely limited to extremely bright sources.

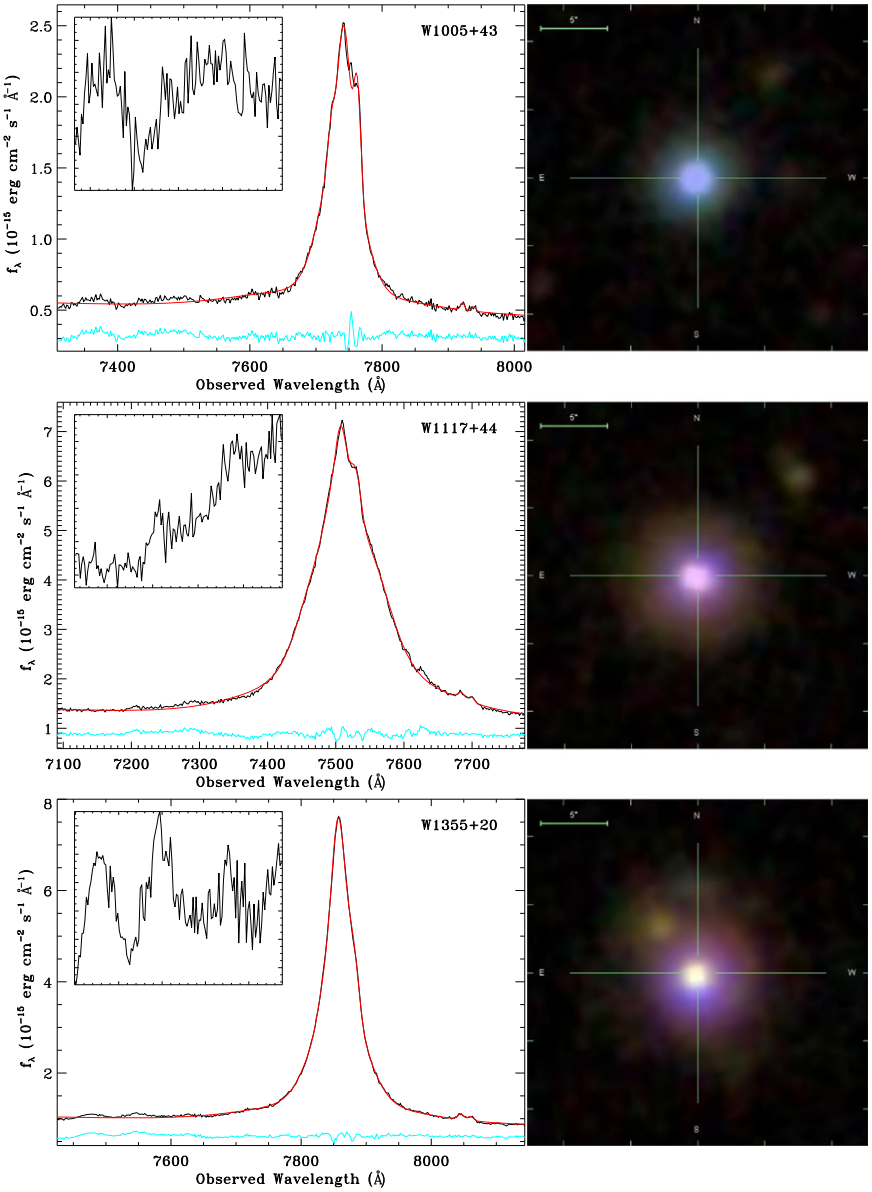

Figure 2. (Continued.)

Finally, Table 5 and Figure 4 may give an impression that [O I]-to-luminosity ratios are higher for the AGN-dominated QSOs (also with higher black hole masses) than for the SB-dominated ones. The average ratio $\langle L_{[\mathrm{O\,I}]63\,\mu\mathrm{m}}/L_{\mathrm{FIR}}\rangle_{\mathrm{AGN}}$ is -2.49 ± 0.14 for all detections, and -2.98 ± 0.22 if we exclude W0752+19 (which is AGN dominated). The same average ratio is only -3.36 ± 0.13 for the SB-dominated QSOs. It is possible that such a trend between $L_{[\mathrm{O\,I}]63\,\mu\mathrm{m}}/L_{\mathrm{FIR}}$ and AGN fraction does exist; however, it is very weak. In addition, the average ratio $\langle L_{[\mathrm{C\,II}]}/L_{\mathrm{FIR}}\rangle$ is -2.90 ± 0.20 and -3.12 ± 0.35 for the AGN- and SB-dominated systems, respectively. These average ratios are statistically the same for the two types of QSOs in our sample.

If the slightly enhanced $L_{[\mathrm{O\,I}]63\,\mu\mathrm{m}}/L_{\mathrm{FIR}}$ ratios among the AGN-dominated systems are real, this trend cannot be true for all AGNs and star-forming galaxies in general. It has to be limited to our selected QSOs that are at similar redshifts with similar L_{IR} and "effective" FIR dust temperature (FIR f_{60}/f_{100} colors). A possible explanation is that AGN-dominated systems, i.e., more massive black holes, tend to have more emission at the mid-IR and much less at the FIR. Table 5 shows that the AGN-dominated targets all have smaller $L_{\mathrm{FIR}}/L_{\mathrm{IR}}$ ratios. On average, smaller L_{FIR} values lead to larger $L_{[\mathrm{O\,I}]63\,\mu\mathrm{m}}/L_{\mathrm{FIR}}$ ratios. However, if this is the only explanation, it is hard to understand why [C II]-to-luminosity ratios are similar among both types of QSOs in our sample. Another possible reason is that AGN-dominated systems may have higher ionizing fluxes from stronger black hole accretion activities, which in turn may produce more excited neutral O atoms, and thus stronger [O I] 63 μm emission, due to the fact that the $J = 1$, 0 levels of the O^0 ground states require 228 K and 327 K energy. This argument has been used by theoretical models (Meijerink & Spaans 2005; Abel et al. 2009) to explain observed [C II]/[O I] ratios. However, the recent paper by Langer & Pineda (2015) has argued differently, that X-rays in AGNs could produce more ions at higher ionization states, thus

Table 4
Photometry

Galaxy (1)	$f_{1.2}$ (2)	$f_{1.6}$ (3)	$f_{2.2}$ (4)	f_{W1} (5)	f_{W2} (6)	f_{W3} (7)	f_{W4} (8)	f_{12} (9)	f_{25} (10)	f_{60} (11)	f_{100} (12)
W0752+19	3.66 ± 0.27	3.52 ± 0.41	6.05 ± 0.48	10.76 ± 0.39	17.37 ± 0.58	48.6 ± 5.7	160 ± 19	…	…	…	…
W0946+13	3.09 ± 0.16	3.87 ± 0.22	6.26 ± 0.29	9.95 ± 0.36	14.91 ± 0.49	45.9 ± 5.3	140 ± 18	…	…	…	…
W1005+43	1.84 ± 0.11	2.59 ± 0.16	5.56 ± 0.26	7.24 ± 0.27	11.77 ± 0.41	49.4 ± 5.7	131 ± 16	<233.6	185 ± 19	558 ± 45	874 ± 131
W1117+44	3.38 ± 0.16	3.97 ± 0.19	7.76 ± 0.31	13.91 ± 0.50	22.90 ± 0.76	58.8 ± 6.7	148 ± 18	110 ± 37	149 ± 33	191 ± 47	200 ± 60
W1355+20	2.73 ± 0.17	4.32 ± 0.28	8.13 ± 0.39	16.62 ± 0.60	24.99 ± 0.85	73.6 ± 8.5	171 ± 21	<341	210 ± 30	264 ± 43	<985
W1422+29	3.30 ± 0.28	3.56 ± 0.38	3.84 ± 0.40	2.35 ± 0.09	2.69 ± 0.09	28.3 ± 3.3	132 ± 16	<203	165 ± 18	960 ± 77	1390 ± 194
W1519+52	1.99 ± 0.13	3.61 ± 0.24	6.91 ± 0.34	11.84 ± 0.42	19.74 ± 0.66	75.9 ± 8.7	220 ± 26	79 ± 18	279 ± 22	780 ± 47	1341 ± 134
W1634+20	3.18 ± 0.35	5.20 ± 0.55	10.20 ± 0.74	15.54 ± 0.56	22.09 ± 0.76	46.0 ± 5.3	119 ± 14	<155	141 ± 11	559 ± 45	1170 ± 199
W1659+18	1.49 ± 0.09	2.31 ± 0.13	4.48 ± 0.22	12.52 ± 0.46	18.82 ± 0.63	56.2 ± 6.4	149 ± 18	<218	163 ± 18	277 ± 42	<1560

Note. Column (1): source; columns (2)–(4): fluxes of the 2MASS J, H, and K_s band, respectively; columns (5)–(8): fluxes of the four *WISE* bands; columns (9)–(12): fluxes of the four *IRAS* bands. Fluxes are in units of mJy.

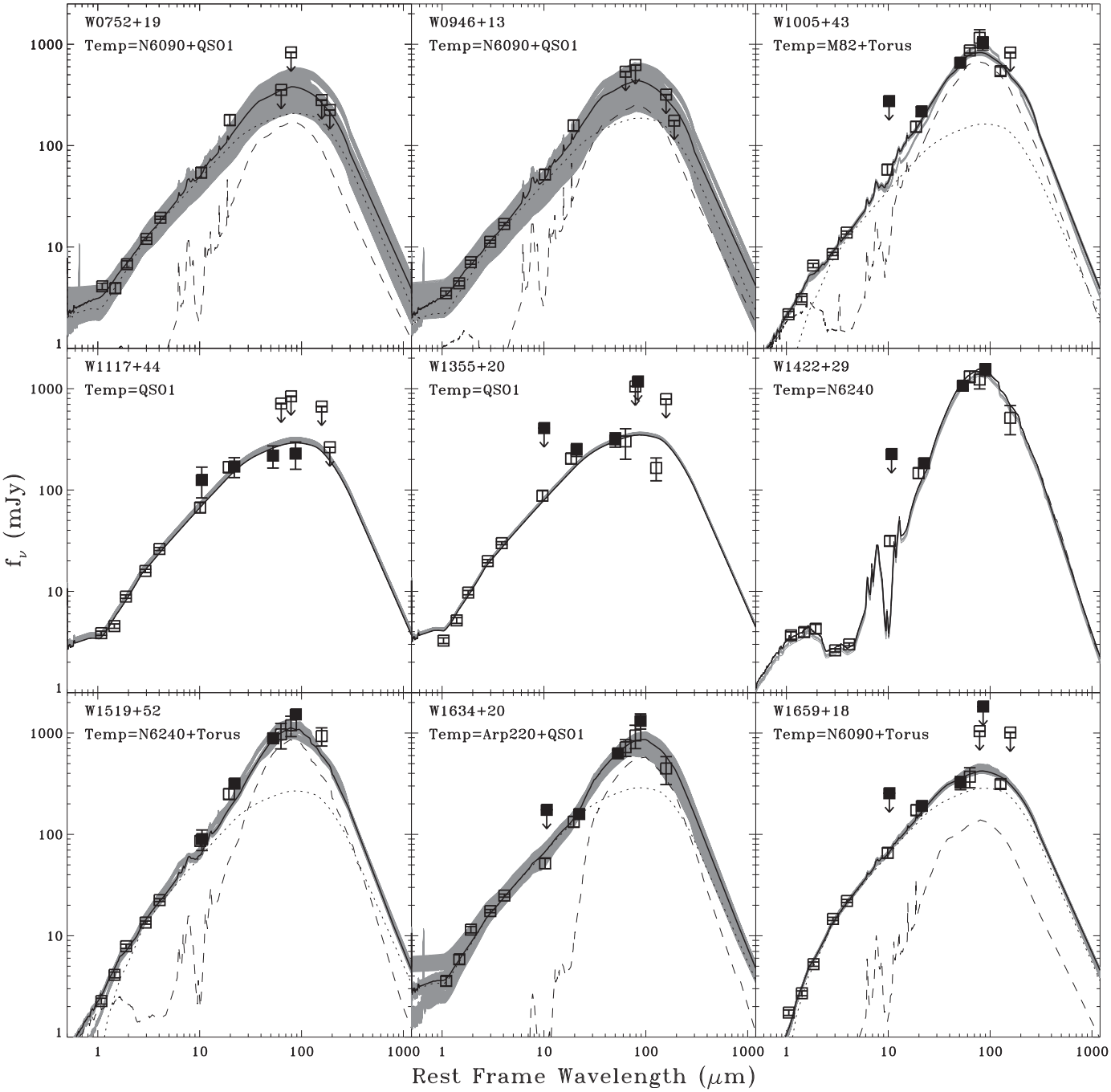

Figure 3. The NIR to FIR SEDs (as listed in Tables 3 and 4) for our sample QSOs. The *IRAS* photometry is plotted as filled squares, and arrows indicate 3σ upper limits. The best-fitted result is shown by the thick solid line, with individual components from SB and AGN templates (as labeled in each panel) of the SWIRE library (Polletta et al. 2007) plotted as dashed and dotted lines, respectively. The gray lines give all model results at the 95% confidence level.

leading to low observed [C II] fluxes among luminous ULIRGs and AGNs. One of our QSOs, W1117+44, has an observed X-ray flux of $(2.24 \pm 0.06) \times 10^{-12}$ erg s^{-1} cm^{2} (Bianchi et al. 2009). Comparing its X-ray luminosity of 1.24×10^{44} erg s^{-1} with the Langer & Pindeda model (their Figure 14), we obtain a higher $L_{[\mathrm{C\,II}]}/L_{\mathrm{FIR}}$ ratio (-2.69, -2.73, and -2.79 for filling factors of 0.003, 0.002, and 0.001, respectively; log scale) than our observed value (<-3.26; log scale). Thus, we conclude that it is not clear at all whether the physical model is valid for explaining [C II] and [O I] emissions from AGNs and galaxies. More observations in the [C II] and [O I] lines and X-ray for AGNs/QSOs would be helpful for understanding this contradiction.

Cross-checking the host galaxy morphologies shown in Figures 2(a) and (b) against the line-to-luminosity ratios, we do not see any definitive correlation. This is probably due to the fact that the FIR line ratios are more sensitive to the FIR surface brightness, rather than directly the optical morphologies (Díaz-Santos et al. 2013). Our sources have typical QSO spectra with optical forbidden emission lines, such as [O III] λ5007 and [O I]$\lambda\lambda$6300, 6364 both coming from the narrow-line regions (NLRs) in these QSOs. The [O III] λ5007/[O I]

Table 5
Derived Properties

Source (1)	$L_{\rm bol}^{\rm QSO}$ ($L_\odot$) (2)	$M_{\rm BH}$ ($M_\odot$) (3)	$L_{\rm IR}$ ($L_\odot$) (4)	$L_{\rm FIR}$ ($L_\odot$) (5)	$f_{\rm SB}$ (6)	$\frac{f_{60}}{f_{100}}$ (7)	$\frac{[\rm O\,I]}{\rm FIR}$ (8)	$\frac{[\rm C\,II]}{\rm FIR}$ (9)	$\frac{[\rm O\,I]}{[\rm C\,II]}$ (10)	$R_{\rm ENLR}$ (kpc) (11)	$M_{\rm dyn}\sin^2 i$ ($M_\odot$) (12)
sW0752[a]	11.87	9.43	11.67	11.16	0.43	0.94	−2.01	−2.70	4.89	3.2	11.6
W0752[a]	...	...	...	...	...	...	−2.56	−2.70	1.39	...	...
W0752[a]	...	...	...	...	...	...	−2.15	<−3.15	>10.0	...	...
W0946	12.08	8.39	11.80	11.33	0.55	0.95	<−3.59	−3.31	<0.52	4.0	11.0
W1005	11.92	7.94	12.27	11.88	0.79	0.97	−3.37	−3.55	1.51	3.4	10.9
W1117	12.13	8.77	11.85	11.26	0.0	0.93	<−3.27	<−3.26	...	4.3	...
W1355	12.30	8.21	12.23	11.63	0.0	0.94	−3.00	−2.90[b]	0.79[b]	5.1	11.7
W1422	11.35	7.52	11.94	11.71	1.0	0.96	−3.29	−3.42	1.34	1.9	10.5
W1519	11.12	8.07	12.12	11.76	0.74	0.95	...	−2.75	...	1.5	10.4
W1634	11.07	8.54	11.96	11.56	0.63	0.86	−3.26	−3.07	0.65	1.4	10.9
W1659	11.46	9.16	12.10	11.57	0.31	0.95	−2.80	−2.91	1.28	2.1	11.1

Notes. Column (1): abbreviated source name; column (2): bolometric luminosity of the QSO adopted from Shen et al. (2011) and corrected for the host contamination using their Equation (1); column (3): black hole mass adopted from Shen et al. (2011); columns (4) and (5): total IR and FIR luminosity obtained from the SED fitting, respectively; column (6): fractional contribution to $L_{\rm FIR}$ from the SB component based on the SED-fitting results; column (7): 60–100 μm flux ratio obtained through the SED fit; columns (8) and (9): logarithm of the [O I]- and [C II]-to-FIR ratios, respectively; column (10): [O I]-to-[C II] ratio; column (11): size of the extended narrow-line region estimated using the continuum luminosity at 5100 Å ($L_{5100\text{Å}}$) and Equation (3) in Husemann et al. (2014); column (12): dynamical mass calculated using $R_{\rm ENLR}$; column (13): size of the broad-line region estimated using L_{5100} and the best-fitted results in Bentz et al. (2009); column (14): dynamical mass calculated using $R_{\rm BLR}$. All luminosities, masses, and line-to-FIR ratios are in logarithmic scale.
[a] The ratios listed in the first, second, and third lines were calculated with line fluxes from the total, narrow, and broad component, respectively.
[b] For the [C II] emission, only the component with similar velocity to [O I] line was used.

λ6300 line ratio is sensitive to the ionization parameter. The higher [O III] λ5007/[O I]λ6300 ratios imply higher fractions of ionized O^{++} atoms and the stronger ionization fields from the central AGNs. Here we use the observed ratio of log([O III] λ5007/Hβ)−log([O I]λ6300/Hα) as a proxy for [O III] λ5007/[O I]λ6300, where the narrow component of Hα and Hβ and both the narrow and broad components of [O III] λ5007 and [O I]λ6300 were used to obtain the ratio. In this way, the dust extinction is essentially taken into account by the ratio of Hα/Hβ. Figure 5 shows the derived [O III] λ5007/[O I]λ6300 ratio versus $L_{[\rm O\,I]63\,\mu m}/L_{\rm FIR}$. From the figure we see a weak anticorrelation between the $L_{[\rm O\,I]63\,\mu m}/L_{\rm FIR}$ and [O III] λ5007/[O I]λ6300 ratios, in the sense that the sources with smaller [O III] λ5007/[O I]λ6300 ratios have a higher fraction of [O I] 63 μm emission. This might indicate that a larger fraction of the ISM is in a neutral phase.

One QSO, W0752+19, has an exceptionally high $L_{[\rm O\,I]63\,\mu m}/L_{\rm FIR}$ ratio, about an order of magnitude higher than that of the other sources in our sample, as well as that of local ULIRGs. Its ratio is also higher than the average value for galaxies at similar $L_{\rm FIR}$. Like some rare cases at low z, the $L_{[\rm O\,I]63\,\mu m}/L_{\rm FIR}$ ratio for W0752+19 is close to the high values observed among high-z SMGs (Coppin et al. 2012) and star-forming galaxies (Brisbin et al. 2015), with $L_{\rm FIR}$ an order of magnitude higher. We discuss how and where such a strong emission is produced in W0752+19 in the following sections.

3.3.2. Comparison to PDR Models

In this section, we compare our observations with standard PDR models published in the literature. Strictly speaking, it is not appropriate to apply standard PDR models to the observations of IR-bright QSOs because AGNs make contributions to both [O I] and [C II] emission, as well as IR continuum luminosity. Although we have done SED decomposition and can measure $L_{\rm IR}$ (SB) and $L_{\rm IR}$ (AGN) separately, we do not have sufficient information to do a similar analysis on [O I] and [C II]. This underscores the urgent need to build suitable models for interpreting FIR fine-structure lines from AGNs/QSOs. With these limitations in mind, we apply Kaufman et al. (1999) PDR models to our data.

[O I]-to-[C II] ratios can be used to constrain ISM density and the strength of the FUV radiation field. The [O I] 63 μm has a much higher critical density for collisional excitation than that for [C II] 158 μm. At the limit of very high density ($n \gg n_{\rm cr,[O\,I]} = 5\times10^5$ cm^{-3}), oxygen cooling is dominant, both species are in local thermodynamic equilibrium, and the ratio of their cooling rates is independent of density. In the low-density limit (diffuse ISM, $n \ll n_{\rm cr,[C\,II]} \sim 3000$ cm^{-3}), both cooling rates scale quadratically with density; thus, the line ratio is independent of n. Only in the intermediate-density regime, $n_{\rm cr,[C\,II]} < n < n_{\rm cr,[O\,I]}$, does the [O I]-to-[C II] ratio depend on density.

One critical feature of the Kaufman et al. (1999) PDR model is that it is built for a two-dimensional slab with infinite length. However, actual observations of distant extragalactic sources usually detect emissions from multiple, three-dimensional PDR regions within a single beam. Such a geometric difference implies the necessary corrections to $L_{[\rm O\,I]63\,\mu m}$, $L_{[\rm C\,II]}$, and $L_{\rm IR}$. To calculate the correct $(L_{[\rm O\,I]63\,\mu m}+L_{[\rm C\,II]})/L_{\rm IR}$ ratios for the model comparison, we use the following equation: $(L_{[\rm O\,I]63\,\mu m}+L_{[\rm C\,II]}/1.4)/(L_{\rm IR}/2.0)$. Here the observed $L_{\rm IR}$ is reduced by a factor of 2. This is because the actual observations detect infrared continuum emission from the front and back side of the clouds, especially when they are illuminated from all sides. In contrast, the 2D slab models only take into account the partial emission. The correction factor of 2 is suggested by Kaufman et al. (1999).

The [O I] 63 μm emission is optically thick; thus, the observed fluxes come from the front side of the clouds. The actual observed value is very similar to the model geometry of 2D slab case. Thus, no corrections are applied to the observed [O I] fluxes. In addition, the observed [C II] emission is also corrected for the geometric effect. As discussed in Kaufman

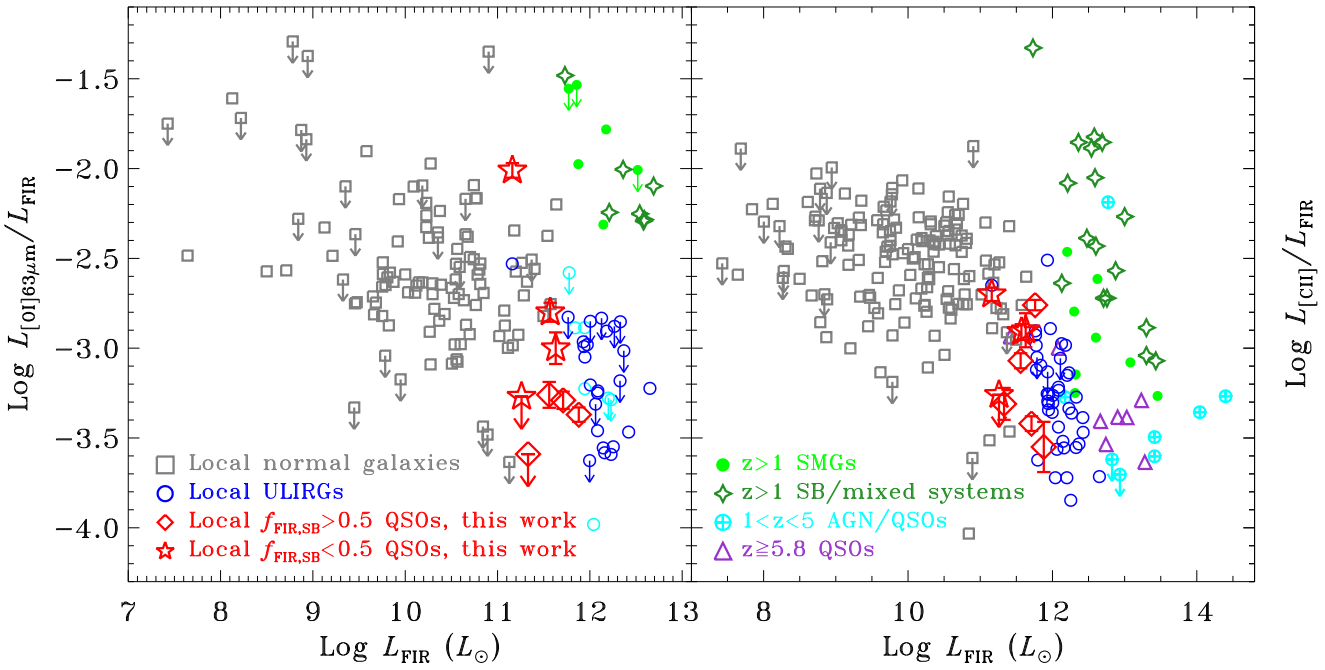

Figure 4. Left: $L_{[O\,I]63\,\mu m}/L_{FIR}$ vs. L_{FIR}. Right: $L_{[C\,II]}/L_{FIR}$ vs. L_{FIR}. Red symbols show QSOs in current work, with open diamonds and five-point stars representing $f_{SB} > 0.5$ and $f_{SB} < 0.5$, respectively. To compare our data with other samples, we also plot local normal galaxies (including LIRGs; Brauher et al. 2008), local ULIRGs (Brauher et al. 2008; Farrah et al. 2013), $z > 1$ star-forming (SB)/mixed systems (Stacey et al. 2010; Brisbin et al. 2015), $z > 2$ submillimeter-bright galaxies (SMGs; Maiolino et al. 2009; Ivison et al. 2010; De Breuck et al. 2011; Valtchanov et al. 2011; Coppin et al. 2012; Swinbank et al. 2012; Wagg et al. 2012; Riechers et al. 2013), $1 < z < 5$ [C II] detected AGNs/QSOs (Pety et al. 2004; Stacey et al. 2010; Gallerani et al. 2012; Wagg et al. 2012), and $z > 5.8$ QSOs (Maiolino et al. 2005; Venemans et al. 2012; Leipski et al. 2013; Wang et al. 2013; Willott et al. 2013).

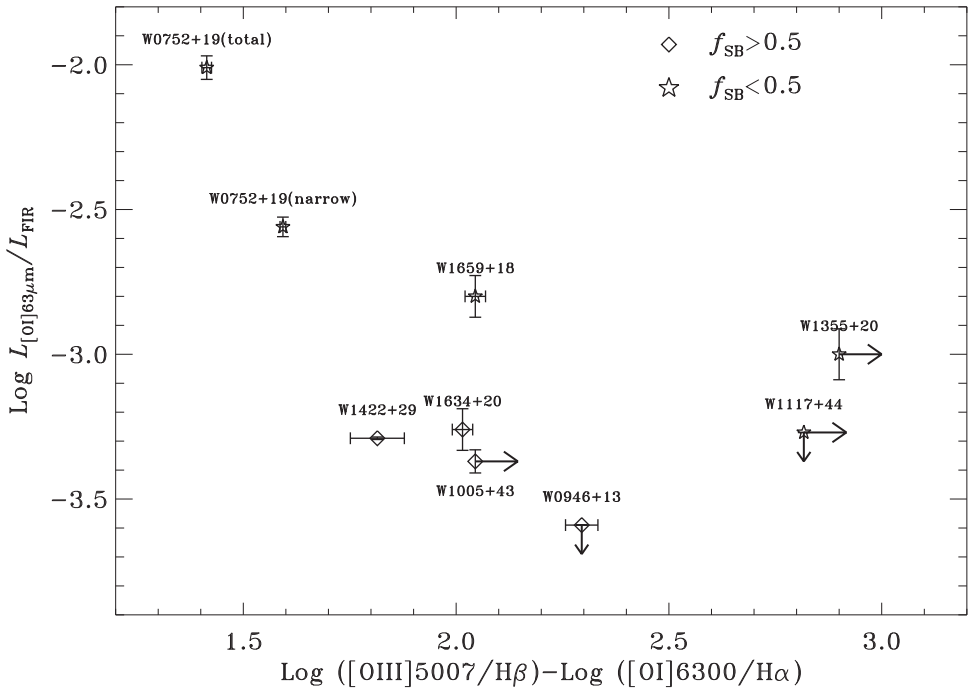

Figure 5. $L_{[O\,I]63\,\mu m}/L_{FIR}$ vs. $L_{O\,[III]\,\lambda5007}/L_{[O\,I]\,\lambda6300}$. The total and narrow components of W0752+19 are plotted separately in this figure.

et al. (1999), [C II] is thought to be marginally optically thick, and its optical depth τ at the line center is close to ~1 (Luhman et al. 2003). Therefore, the observed [C II] fluxes include emission mostly from the front side and some from the back side of the clouds. The observed values are $(1.0 + e^{-\tau})$ times that from a 2D model, i.e., the observed fluxes divided by 1.4 when compared with 2D models. However, this method is not always adopted in the published literature (e.g., Malhotra et al. 2001). Partly this is due to the complex nature of the problem, where many factors such as optical depths, filling

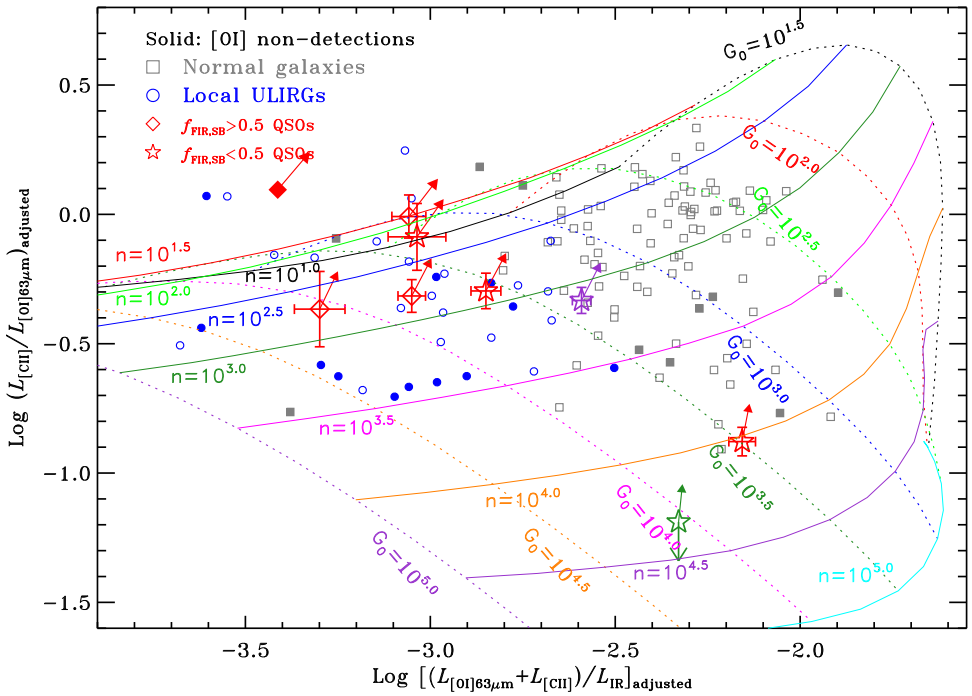

Figure 6. Observed data points overlaid on the PDR model grid (Kaufman et al. 1999); dotted and solid lines correspond to constant strength of radiation field (G_0) and number density (n), respectively. The various geometric corrections have been applied to the observed [C II] and L_{IR} values (see the text for details). Red symbols show QSOs in this work, with diamonds and stars representing $f_{SB} > 0.5$ and $f_{SB} < 0.5$, respectively. Solid arrows associated with our QSOs give the locations when the correction factor of 1.4 is not applied to the [C II] flux. Solid symbols indicate that the [O I] 63 μm line is undetected. The purple and green stars respectively show the narrow and broad components (but without splitting the IR flux) of W0752+19. In this figure we also plot local normal galaxies (including LIRGs; Brauher et al. 2008) and local ULIRGs (Brauher et al. 2008; Farrah et al. 2013) for comparisons.

factors, etc., can easily affect the observed fluxes, whereas PDR models are still fairly simple. In a later section, we also compare our observations with PDR models without correcting observed [C II] fluxes.

Finally, one more correction applied to the observed [C II] emission is to remove the contribution from extended, ionized gas. For this correction, we have utilized the relation between the ratio ([C II]/[N II] 205 μm) of the [C II] to [N II] 205 μm emission and f_{60}/f_{100} (Lu et al. 2015) and adopted solar gas phase abundances of C/H = 1.4×10^{-4} and N/H = 7.9×10^{-5} (Savage & Sembach 1996). Because of the similar ionization potentials and the same critical densities (for collision partner of electron) for [C II] and [N II] 205 μm lines, the [C II]/[N II]205 μm ratio, which is independent of the density and mildly dependent on the ionization field intensity, can estimate the fraction of the [C II] emission from ionized gas, based only on an assumed gas phase C/N abundance ratio (e.g., Oberst et al. 2006; Stacey et al. 2010). Here we adopt log [N II]205 μm/[C II] = $-0.65 f_{60}/f_{100} - 0.66$, which was obtained based on the observations of local (U)LIRGs (Lu et al. 2015). For our sample QSOs, the average [C II] fraction from the ionized medium is ~0.1. Finally, we want to caution readers that these correction factors are uncertain and that non-PDR components (e.g., dusty ionized regions) might also contribute to the FIR continuum, especially for high-G_0 sources (e.g., Luhman et al. 2003; Abel et al. 2009).

Figure 6 shows the comparison between the data and the calculated grid of density n_0 and FUV radiation field G_0 using the Kaufman et al. (1999) models. By assuming a local Galactic metallicity, these models were computed for a grid of density n and FUV radiation field G_0 parameters with n = 10^1–10^7 cm^{-3} and G_0 = $10^{-0.5}$–$10^{6.5}$ in units of the local interstellar value, 1.6×10^{-3} erg cm^{-2} s^{-1} (Habing 1968). In Table 6 we listed the derived values of n and G_0, using the web-based tool PDR Toolbox[8] (Kaufman et al. 2006; Pound & Wolfire 2008). The uncertainties were obtained using Monte Carlo simulations by assuming a Gaussian error. In the table we also gave the results for which the AGN contribution to L_{IR} was removed.

Excluding W0752+19, our sample has $n < \sim 10^3$ cm^{-3} and the FUV radiation fields of $10^3 \lesssim G_0 \lesssim 10^{4.2}$. Figure 6 also compares our sample with local ULRIGs and normal star-forming galaxies. It is clear that the ISM in our QSO sample has similar density and FUV radiation field (G_0) to those in local Seyfert 1 ULIRGs (e.g., Farrah et al. 2013), but has much higher G_0 values than that of normal star-forming galaxies. The higher G_0 values in QSOs and ULIRGs are expected due to the central powerful AGNs and/or compact nuclear SB regions.

The exceptional source in our sample is W0752+19, which shows two components in its [O I] 63 μm emission (Table 5) and appears to be an "outlier" in the $L_{[O\,I]63\,\mu m}/L_{FIR}$–$L_{FIR}$ relation (Figure 4). The [O I] broad velocity component does not have a corresponding broad [C II] component, detectable in our spectra. In Figure 6, we plot both components separately, where the 3σ upper limit for the [C II] broad component was adopted. Please note that we do not split the IR flux since it is hard to do it in a fair way. Compared with the model grid, the narrow velocity component for W0752+19 has very similar properties to that of the rest of the sample with $n \sim 10^{3.3}$ cm^{-3} and $G_0 \sim 10^{3.5}$. However, the ISM of the broad velocity component has a density of $>10^{4.3}$ cm^{-3}, much denser than any

[8] http://dustem.astro.umd.edu/pdrt/

Table 6
Results from PDR Modeling

Galaxy (1)	log n (cm^{-3}) (2)	log G_0 (1.6×10^{-3} erg cm^{-2} s^{-1}) (3)	log n (cm^{-3}) (4)	log G_0 (1.6×10^{-3} erg cm^{-2} s^{-1}) (5)
W0752+19 (narrow)	3.25 ± 0.09	3.50 ± 0.08	3.50 ± 0.29	2.75 ± 0.17
W0752+19 (broad)	>4.25	~4.0	>5.25	~1.0
W0752+19 (total)	4.0 ± 0.20	3.50 ± 0.17	4.75 ± 0.16	0.75 ± 11
W0946+13	<1.5	<3.25	<1.5	<2.75
W1005+43	3.00 ± 0.17	4.25 ± 0.28	3.00 ± 0.28	4.00 ± 0.28
W1355+20[a,b]	1.25	2.5	…	…
W1422+29[c]	2.75 ± 0.21	3.75 ± 0.17	2.75 ± 0.21	3.75 ± 0.17
W1634+20[a]	1.5	2.75 ± 0.59	2.5	3.00 ± 0.22
W1659+18	2.75 ± 0.22	3.50 ± 0.12	3.25 ± 0.35	2.75 ± 0.20

Notes. Column (1): source; columns (2) and (3): density and FUV radiation field, respectively; columns (4) and (5): density and FUV radiation field, respectively, with IR only from the SB component.
[a] Values without errors mean that the uncertainty is very large since the observed data fall in regions where the PDR models show complicated behavior (see Figure 6).
[b] The AGN contribution to L_{IR} is 100% and thus no fit to the SB component only.
[c] The SB contribution to L_{IR} is 100%.

of the local ULIRGs and normal galaxies, but reaching similar values observed among a few SB galaxies at $z > 1$.

In Figure 6 we also use solid arrows to indicate the locations (i.e., the arrow head) of our QSOs when the correction factor of 1.4 is not applied to the [C II] flux. A source will move along both axes by 0.15 dex when the [C II] emission dominates the cooling, and thus the estimated n and G_0 will lower by 0.1–0.3 dex. It is important to note that in the regimes with very low or high n values, small changes in line flux ratios could imply significant changes in the inferred density values from comparisons with models, as shown in Figure 6. However, one should be cautious because PDR models may not be very reliable in these regimes. Considering that these n and G_0 values are rough estimates, we believe that applying the correction factor of 1.4 to the [C II] flux or not will not affect the main science conclusions in this paper.

3.4. Origin of the FIR [O I] and [C II] Emissions

3.4.1. Is Shock/Turbulence an Important Heating Source?

The FIR fine-structure lines [O I] 63 μm and [C II] are thought to be excited by collisions with atomic and molecular hydrogen in PDRs, where the gas is heated by the photoelectric effect, i.e., hot electrons are ejected from PAH molecules and small dust grains by absorbing FUV photos, and they transfer their energy to the gas. [O I]$\lambda\lambda$6300, 6364 and [O I] 63 μm emissions can also be produced or boosted by shocks (Hollenbach & McKee 1989; Allen et al. 2008; Lesaffre et al. 2013) in the outflows/winds observed frequently in both nearby and distant QSOs (Greene et al. 2011; Nesvadba et al. 2011; Sturm et al. 2011; Cano-Díaz et al. 2012; Harrison et al. 2012).

Specifically for the objects in our sample, the question is whether any observed FIR fine-structure emission could have different heating sources, particular the ones with broad velocity components. Could the dissipation of kinematic energy released through a cascade of turbulent motions from large to small scales be a significant heating source?

To this end, we compared the observed [O I]λ6300/Hα ratios for the narrow component (i.e., FWHM < 1200 km s^{-1}) to the radiative shock models presented in Allen et al. (2008), as shown in Figure 7. We have chosen the model grids that have twice solar abundance and preshock density of $n = 1$ cm^{-3}, as discussed in Allen et al. (2008), because the photoionization models with this metallicity can well reproduce the observed narrow-line ratios in AGNs (Groves et al. 2004, 2006), and AGNs are typically hosted in galaxies more massive than $10^{10}\,M_{\odot}$ and hence are likely to contain high-metallicity gas (e.g., Tremonti et al. 2004). From Figure 7 we can see that shock models fall much too short to match the observed [O I]$\lambda\lambda$6300, 6364 ratios, and the optical [O I] $\lambda\lambda$6300, 6364 emissions are likely powered by FUV photons from AGNs rather than shocks.

In addition, observations and shock model calculations (Burton et al. 1990; Appleton et al. 2013; Lesaffre et al. 2013) have shown that [O I]/FIR and [C II]/FIR ratios for shocked gas tend to be elevated, about an order of magnitude higher than those produced by photoelectric heating in PDRs. As shown in Section 3.3, the observed [O I]/FIR ([C II]/FIR) ratios for our QSOs do not show any significant enhancement comparing to normal/SB/AGN galaxies, which further confirms that the gas emissions, in both the optical and FIR, should be heated by AGNs and/or SB activities of the host galaxies.

3.4.2. Where Do FIR Fine-structure Lines Come From?

The basic result from our study is the detection of strong [O I] 63 μm and [C II] line emission from $z \sim 0.15$ IR-bright QSOs. Using the FIR line-to-luminosity ratios and the standard PDR models, we infer that the densities of the warm neutral gas clouds responsible for the observed line emission are in the range of 10–10^3 cm^{-3}, with one exceptional case of W0752 +19, whose broad [O I] 63 μm component implies a density $>10^{4.3}$ cm^{-3}.

Sources with FIR [O I] 63 μm line widths as broad as 720 km s^{-1} are rare. In the sample of local ULIRGs, Farrah et al. (2013) have found that about 30% have broad components with velocity widths of ~500 km s^{-1}; none reached the level of 700 km s^{-1}. So where does this broad velocity component in W0752+19 come from? There are three possibilities. The first is an NLR with a size of a few hundred parsecs, photoionized by the radiation field of an accreting supermassive black hole. The other two possibilities are star-

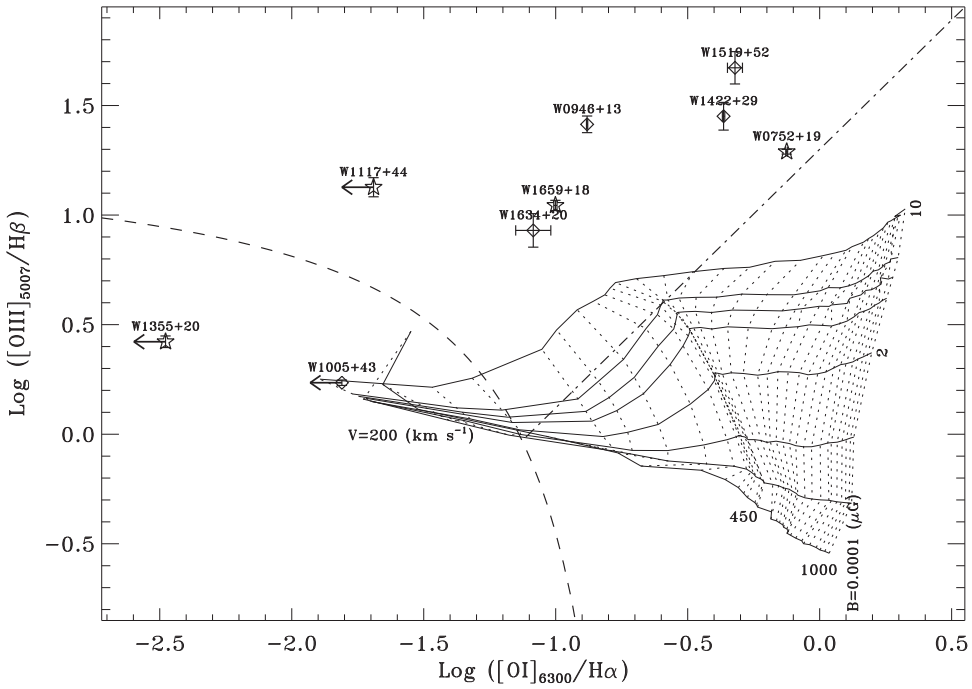

Figure 7. Comparison of the observed ratios to the fast shock model grids with twice solar abundance and preshock density of $n = 1$ cm^{-3} (Allen et al. 2008) on the [O I]λ6300/Hα vs. [O III] λ5007/Hβ diagram. Diamonds and stars represent $f_{\rm SB} > 0.5$ and, respectively. Solid and dotted lines represent constant magnetic field ($B = 10^{-4}$, 0.5, 1.0, 2.0, 3.23, 4.0, 5.0, and, 10.0 μG) and shock velocity ($v = 200$–1000 km^{-1}), respectively. The dashed line represents the Kewley et al. (2001) SB/AGN classification line, while the dot-dashed line shows the Seyfert–LINER division given by Kewley et al. (2006).

forming regions (PDRs) in the host galaxy and dense gas outflows.

In the standard AGN/QSO model, the forbidden emission lines are collisionally excited and believed to come from NLRs with densities of 10^3–10^5 cm^{-3} (see a review by Osterbrock 1991). Most of our FIR [O I] and [C II] detections indicate smaller densities, which suggest that these narrow lines may be mostly coming from the PDRs in the host galaxies. With the same density argument, it would be consistent if the broad [O I] 63 μm component in W0752+19 comes from the warm and dense ISM within the NLR. In addition, we find that the line centroids of broad FIR [O I] and broad optical [O I]λ6300 are coinciding, with the negligible offset of 63 km s^{-1}. This lends additional support to the NLR origin for the broad [O I] 63 μm emission in W0752+19. However, we note that the densities derived here are based on PDR models, which could be significantly different from those derived from an NLR model/geometry. Therefore, we cannot totally rule out the NLR origin of these FIR fine-structure lines.

Gas outflows could be an alternative explanation since outflows are frequently observed in QSOs (e.g., Fischer et al. 2010; Aalto et al. 2012; Cicone et al. 2014; Tadhunter et al. 2014). The broad and asymmetric (e.g., extended blue wing) line profile seems to support this interpretation. The nondetection of the broad [C II] emission line in W0752+19 means that the gas density of this outflow gas is quite high, $\geqslant 10^4$ cm^{-3} (see Section 3.3.2). At these high-density regimes, [C II] emission is suppressed due to collisional de-excitation. Such dense gas outflow is rare and has been reported in Mrk 231 (Aalto et al. 2012). However, one potential difficulty in the outflow scenario is that we do not detect optical [O I] λ6300 emission with a velocity width similar to the broad [O I] 63 μm component in W0752+19.

3.5. Implied Dynamical Masses

There is another indirect and crude way to investigate the physical regime where the FIR [O I] ([C II]) emission may arise, i.e., to compare the dynamical mass estimates of the dense neutral gas ($M_{\rm dyn}$) for our sample with those having high spatial resolution observations, such as the high-z QSOs in Wang et al. (2013), in which the [C II] emissions were marginally resolved. Our QSOs have similar black hole masses ($M_{\rm BH}$) to those in Wang et al. (2013). This comparison may shed some light on the properties of the neutral ISM in low- and high-z QSOs.

Many studies of AGNs/QSOs have proposed that NLRs could contain multiple components—an inner biconical NLR over a size of a few hundred parsecs, and a much larger extended narrow-line region (ENLR), which are gravity dominated and could have organized velocity structures, such as outflows and rotations (Osterbrock 1991; Veilleux 1991). For a rotating gas disk with a radius R, the dynamical mass can be calculated as $M_{\rm dyn} = Rv_{\rm cir}^2/G$, where $v_{\rm cir}$ is the maximum circular velocity and G the gravitational constant. Because almost all of the detected [O I] 63 μm and [C II] lines are resolved, as shown in Table 2, it is possible for us to construct a toy model, where we assume that the neutral gas producing FIR [O I] and [C II] emission is in a rotating disk with a radius of the size of ENLR, and we also approximate $v_{\rm cir} \sim$ FWHM(line)/sin i, with i as the disk orientation angle. We chose the larger value of the [O I] 63 μm and [C II] line widths for $v_{\rm cir}$. The ENLR sizes can be estimated using the empirical $L_{5100\text{Å}}$–size relations, $\log(R_{\rm ENLR}\,[\rm pc]) = 0.46\log(L_{5100\text{Å}}\,[\rm erg\ s^{-1}]) - 16.95$ (Bentz et al. 2009; Husemann et al. 2014). The $L_{5100\text{Å}}$ and black hole mass measurements are taken from Shen et al.

(2011). The resulting ENLR radii are 1.4–5.1 kpc, which are comparable to sizes of host galaxies. This toy model yields dynamical masses $M_{\rm dyn}\sin^2 i$ of (2.5–40) $\times 10^{10}\,M_\odot$.

Is this toy model consistent with the gas densities derived from the [O I] 63 μm/[C II] ratios? As we showed before, the gas densities are mostly in the range of $10-10^3\,{\rm cm}^{-3}$. If we take the gas density of $10^3\,{\rm cm}^{-3}$, the disk scale height H of 200 pc, the gas disk with the radii of ENLRs, and the volume filling factor of 0.1, we obtain the total gas masses $M_{\rm H+H_2}=\pi R^2 H\mu_{\rm H} m_{\rm H} n_{\rm H}=4\times10^9$–$5\times10^{10}\,M_\odot$, with $\mu_{\rm H}=1.3$ as the mean atomic weight for neutral gas. These numbers are somewhat smaller, but consistent with the dynamical estimates.

How are our dynamical mass estimates compared with the measurements for high-z QSOs? Wang et al. (2013) recently published a sample of $z\sim5$ QSOs with the ALMA [C II] maps that spatially resolved [C II]-emitting gas, yielding the sizes of 2.6–5.3 kpc. Their derived $M_{\rm dyn}\sin^2 i$ are in the range of (1.6–15) $\times 10^{10}\,M_\odot$ using the same definition of $v_{\rm cir}$ as ours. This is similar to the dynamical gas masses derived for our QSOs. At face value, this similarity implies that the masses of the dense neutral ISM are not changing significantly in QSOs at $z\sim0.15$ and $z\sim5$. This inference seems to be in contradiction with other published ISM studies, suggesting that high-z sources have higher gas fractions relative to their stellar masses (Tacconi et al. 2013; Genzel et al. 2015). This contradiction implies that our assumption of radii R in our calculation may be too large, i.e., the sizes of the FIR line-emitting regions in low-z QSOs are likely smaller than those of ENLRs, 1.4–5.1 kpc. Future high spatial observations are required to confirm our speculations.

4. SUMMARY

We present *Herschel* PACS spectroscopic observations of a sample of nine QSOs, selected to be at $z\sim0.1$–0.2 from SDSS spectra and to have 22 μm fluxes greater than 1 mJy. The full IR SED fitting reveals that our QSOs are mostly SB and AGN composite systems, with $L_{\rm FIR}$ around several times $10^{11}\,L_\odot$, a factor of a few less than that of local ULIRGs and over an order of magnitude less luminous than that of $z>1$ QSOs with available FIR spectroscopy. Our PACS/*Herschel* observations detect strong [O I] 63 μm and [C II] 158 μm emission and discover one object, W0752+19, with exceptionally strong [O I] 63 μm emission and a broad component (720 km s^{-1}). We find that the observed [O I] 63 μm/FIR and [C II]/FIR ratios have similar distributions to those of local ULIRGs, but much higher than those of $z>1$ QSOs/AGNs, with an order of magnitude higher FIR luminosities. Our observations also suggest that the AGN-dominated systems in our sample seem to have higher [O I] 63 μm/FIR ratios, which can be explained by the hotter SEDs produced by AGNs, and by the lower $L_{\rm FIR}/L_{\rm IR}$ ratios in these systems.

Assuming that the [O I] 63 μm and [C II] lines arise mainly in PDRs, we use theoretical models to constrain the hydrogen density, n, and FUV radiation field, G_0, in the FIR line-emitting gas. We find $n\lesssim10^{3.3}\,{\rm cm}^{-3}$ and $10^3\lesssim G_0\lesssim10^{4.2}$ for all systems except for the broad component emitting gas of W0752+19, which has $n\gtrsim10^{4.3}\,{\rm cm}^{-3}$ and $G_0>10^4$. The former ranges of n and G_0 are consistent with those found in local Seyfert 1 ULIRGs (Farrah et al. 2013). Our analysis of the optical [O I]λ6300 emission suggests that shocks do not contribute significantly to the gas heating in our QSO sample.

We thank the anonymous referee for her/his careful reading of the manuscript and the constructive comments/suggestions, which have helped to improve the paper. We also thank Dr. M. G. Wolfire for helpful discussion. Y.Z. is partially supported by the National Natural Science Foundation of China under grant nos. 11390373 and 11420101002, and the CAS pilot-b project #XDB09000000. This research has made use of the NASA/IPAC Extragalactic Database (NED), which is operated by the Jet Propulsion Laboratory, California Institute of Technology, under contract with the National Aeronautics and Space Administration. This publication makes use of data products from the *Wide-field Infrared Survey Explorer*, which is a joint project of the University of California, Los Angeles, and the Jet Propulsion Laboratory/California Institute of Technology, funded by the National Aeronautics and Space Administration. This paper also utilized the publicly available SDSS data sets. Funding for the SDSS and SDSS-II has been provided by the Alfred P. Sloan Foundation, the Participating Institutions, the National Science Foundation, the US Department of Energy, the National Aeronautics and Space Administration, the Japanese Monbukagakusho, the Max Planck Society, and the Higher Education Funding Council for England. The SDSS Web site is http://www.sdss.org/. The SDSS is managed by the Astrophysical Research Consortium for the Participating Institutions. The Participating Institutions are the American Museum of Natural History, Astrophysical Institute Potsdam, University of Basel, University of Cambridge, Case Western Reserve University, University of Chicago, Drexel University, Fermilab, the Institute for Advanced Study, the Japan Participation Group, Johns Hopkins University, the Joint Institute for Nuclear Astrophysics, the Kavli Institute for Particle Astrophysics and Cosmology, the Korean Scientist Group, the Chinese Academy of Sciences (LAMOST), Los Alamos National Laboratory, the Max-Planck-Institute for Astronomy (MPIA), the Max-Planck-Institute for Astrophysics (MPA), New Mexico State University, Ohio State University, University of Pittsburgh, University of Portsmouth, Princeton University, the United States Naval Observatory, and the University of Washington.

REFERENCES

Aalto, S., Garcia-Burillo, S., Muller, S., et al. 2012, A&A, 537, A44
Abel, N. P., Dudley, C., Fischer, J., Satyapal, S., & van Hoof, P. A. M. 2009, ApJ, 701, 1147
Ahn, C. P., Alexandroff, R., Prieto, C. A., et al. 2014, AJ, 211, 17
Allen, M. G., Groves, B. A., Dopita, M. A., Sutherland, R. S., & Kewley, L. J. 2008, ApJS, 178, 20
Appleton, P. N., Guillard, P., Boulanger, F., et al. 2013, ApJ, 777, 66
Bentz, M. C., Peterson, B. M., Pogge, R. W., & Vestergaard, M. 2009, ApJL, 694, L166
Bianchi, S., Guainazzi, M., Matt, G., Fonseca Bonilla, N., & Ponti, G. 2009, A&A, 495, 421
Brauher, J. R., Dale, D. A., & Helou, G. 2008, ApJS, 178, 280
Brisbin, D., Ferkinhoff, C., Nikola, T., et al. 2015, ApJ, 799, 13
Burton, M. G., Hollenbach, D. J., Haas, M. R., & Erickson, E. F. 1990, ApJ, 355, 197
Cano-Díaz, M., Maiolino, R., Marconi, A., et al. 2012, A&A, 537, L8
Capak, P. L., Carilli, C., Jones, G., et al. 2015, Natur, 522, 455
Cicone, C., Maiolino, R., Sturm, E., et al. 2014, A&A, 562, A21
Coppin, K. E. K., Danielson, A. L. R., & Geach, J. E. 2012, MNRAS, 427, 520
De Breuck, C., Maiolino, R., Caselli, P., et al. 2011, A&A, 530, L8
Decarli, R., Walter, F., Carilli, C., et al. 2014, ApJ, 782, 78
Díaz-Santos, T., Armus, L., Charmandaris, V., et al. 2013, ApJ, 774, 68
Farrah, D., Lebouteiller, V., Spoon, H. W. W., et al. 2013, ApJ, 776, 38
Fischer, J., Abel, N. P., González-Alfonso, E., et al. 2014, ApJ, 795, 117
Fischer, J., Sturm, E., González-Alfonso, E., et al. 2010, A&A, 518, L41

Gallerani, S., Neri, R., Maiolino, R., et al. 2012, A&A, 543, 114
Genzel, R., Tacconi, L. J., Lutz, D., et al. 2015, ApJ, 800, 20
Greene, J. E., Zakamska, N. L., Ho, L. C., & Barth, A. J. 2011, ApJ, 732, 9
Groves, B. A., Cecil, G., Ferruit, P., & Dopita, M. A. 2004, ApJ, 611, 786
Groves, B. A., Dopita, M. A., & Sutherland, R. S. 2006, A&A, 458, 405
Habing, H. J. 1968, Bull. Astron. Inst. Netherlands, 19, 421
Harrison, C. M., Alexander, D. M., Swinbank, A. M., et al. 2012, MNRAS, 426, 1073
Hollenbach, D., & McKee, C. F. 1989, ApJ, 342, 306
Husemann, B., Jahnke, K., Sánchez, S. F., et al. 2014, MNRAS, 443, 755
Ivison, R. J., Swinbank, A. M., Swinyard, B., et al. 2010, A&A, 518, L35
Kaufman, M. J., Wolfire, M. G., & Hollenbach, D. J. 2006, ApJ, 644, 283
Kaufman, M. J., Wolfire, M. G., Hollenbach, D. J., & Luhman, M. L. 1999, ApJ, 527, 795
Kessler, M. F., Steinz, J. A., Anderegg, M. E., et al. 1996, A&A, 315, L27
Kessler, M. F., Mueller, T. G., Leech, K., et al. 2003, The ISO Handbook, Vol. I: Mission & Satellite Overview (Noordwijk: ESA) Ver. 2.0
Kewley, L. J., Dopita, M. A., Sutherland, R. S., Heisler, C. A., & Trevena, J. 2001, ApJ, 556, 121
Kewley, L. J., Groves, B., Kauffmann, G., & Heckman, T. 2006, MNRAS, 372, 961
Langer, W. D., & Pineda, J. L. 2015, A&A, 580, A5
Leipski, C., Meisenheimer, K., Walter, F., et al. 2013, ApJ, 772, 103
Lesaffre, P., Pineau des Forêts, G., Godard, B., et al. 2013, A&A, 550, A106
Lu, N., Zhao, Y., Xu, C. K., et al. 2014, ApJL, 787, L23
Lu, N., Zhao, Y., Xu, C. K., et al. 2015, ApJL, 802, L11
Luhman, M. L., Satyapal, S., Fischer, J., et al. 2003, ApJ, 594, 758
Lupton, R., Blanton, M. R., Fekete, G., et al. 2004, PASP, 116, 133
Maiolino, R., Caselli, P., Nagao, T., et al. 2009, A&A, 500, L1
Maiolino, R., Cox, P., Caselli, P., et al. 2005, A&A, 440, L51
Malhotra, S., Kaufman, M. J., Hollenbach, D., et al. 2001, ApJ, 561, 766
Meijerink, R., & Spaans, M. 2005, A&A, 436, 397
Muñoz-Mateos, J. C., et al. 2009, ApJ, 703, 1569
Nesvadba, N. P. H., Polletta, M., Lehnert, M. D., et al. 2011, MNRAS, 415, 2359
Oberst, T. E., Parshley, S. C., Stacey, G. J., et al. 2006, ApJL, 652, L125
Osterbrock, D. E. 1991, PASP, 103, 874
Ott, S. 2010, in ASP Conf. Ser. 434, Astronomical Data Analysis Software and Systems XIX, ed. Y. Mizumoto, K.–I. Morita, & M. Ohishi (San Francisco, CA: ASP), 139
Pety, J., Beelen, A., Cox, P., et al. 2004, A&A, 428, L21
Pilbratt, G. L., Riedinger, J. R., Passvogel, T., et al. 2010, A&A, 518, L1
Poglitsch, A., Waelkens, C., Geis, N., et al. 2010, A&A, 518, L2
Polletta, M., Tajer, M., Maraschi, L., et al. 2007, ApJ, 663, 81
Pound, M. W., & Wolfire, M. G. 2008, in ASP Conf. Ser. 394, Astronomical Data Analysis Software and Systems XVII, ed. R. W. Argyle, P. S. Bunclark, & J. R. Lewis (San Francisco, CA: ASP), 654
Riechers, D. A., Bradford, C. M., Clements, D. L., et al. 2013, Natur, 496, 329
Sargsyan, L., Samsonyan, A., Lebouteiller, V., et al. 2014, ApJ, 790, 15
Savage, B. D., & Sembach, K. R. 1996, ARA&A, 34, 279
Sawicki, M. 2012, PASP, 124, 1208
Schneider, D. P., Richards, G. T., Hall, P. B., et al. 2010, AJ, 139, 2360
Shen, Y., Richards, G. T., Strauss, M. A., et al. 2011, ApJS, 194, 45
Spergel, D. N., Bean, R., Doré, O., et al. 2007, ApJS, 170, 377
Stacey, G. J., Geis, N., Genzel, R., et al. 1991, ApJ, 373, 423
Stacey, G. J., Hailey-Dunsheath, S., Ferkinhoff, C., et al. 2010, ApJ, 724, 957
Sturm, E., GonzáLez-Alfonso, E., Veilleux, S., et al. 2011, ApJL, 733, L16
Swinbank, A. M., Karim, A., Smail, I., et al. 2012, MNRAS, 427, 1066
Tacconi, L. J., Neri, R., Genzel, R., et al. 2013, ApJ, 768, 74
Tadhunter, C., Morganti, R., Rose, M., Oonk, J. B. R., & Oosterloo, T. 2014, Natur, 511, 440
Tielens, A. G. G. M., & Hollenbach, D. 1985, ApJ, 291, 722
Tremonti, C. A., Hechkman, T. M., Kauffmann, G., et al. 2004, ApJ, 613, 898
Valtchanov, I., Virdee, J., Ivison, R. J., et al. 2011, MNRAS, 415, 3473
Veilleux, S. 1991, ApJ, 369, 331
Venemans, B. P., McMahon, R. G., Walter, G., et al. 2012, ApJL, 751, L25
Wagg, J., Wiklind, T., Carilli, C., et al. 2012, ApJL, 752, L30
Wang, R., Wagg, J., & Carilli, C. L. 2013, ApJ, 773, 44
Willott, C. J., Omont, A., & Bergeron, J. 2013, ApJ, 770, 13
Wright, E. L., Eisenhardt, P. R. M., Mainzer, A. K., et al. 2010, AJ, 140, 1868
Zhao, Y., Lu, N., Xu, C. K., et al. 2013, ApJL, 765, L13
Zhao, Y., Lu, N., Xu, C. K., et al. 2016, ApJ, 819, 69